Analysis of the Effects of Pre-whirl on the Efficiency and Operating Range of Hydro Pumps used in Pumped Storage Facilities

Keith A. Martin[12*]

Abstract
This paper discusses the application of computational fluid dynamics (CFD) to a case study of a hydraulic pump turbine operating in pumping mode. Emphasis is on the effects of induced pre-whirl on flow patterns through the impeller and on pump performance. ANSYS® Fluent, Academic Research, Release 14.0, software is used to model three-dimensional (3D) Reynolds-averaged Navier-Stokes (RANS) equations with a $k-\omega$ SST turbulence model. Full-wheel fixed rotor simulations are used to identify operating parameters that are used in more computationally intensive full-wheel moving mesh simulations.

Keywords
pumped storage - hydraulic pump turbine - hydroelectic generation - numerical simulation - computational fluid dynamics - CFD - flow prediction

[1] *The Graduate School, Department of Mechanical and Nuclear Engineering, The Pennsylvania State University*
[2] *Hydro Research Foundation Fellow*
*__Thesis Advisor__: John M. Cimbala, Professor of Mechanical Engineering, The Pennsylvania State University

Contents

Nomenclature

Latin Symbols

b	Runner outlet passage reference height	[m]
c_p	Pressure coefficient: $c_p = \frac{p-p_{ref}}{\frac{1}{2}\rho U_{ref}^2}$	[-]
C	Absolute velocity	$[\mathrm{m}\cdot\mathrm{s}^{-1}]$
C_r	Absolute radial velocity	$[\mathrm{m}\cdot\mathrm{s}^{-1}]$

C_θ	Absolute azimuthal velocity	$[\mathrm{m}\cdot\mathrm{s}^{-1}]$
C_z	Absolute axial velocity	$[\mathrm{m}\cdot\mathrm{s}^{-1}]$
c^*	Nondimensional absolute velocity	[-]
c_r^*	Nondimensional absolute radial velocity	[-]
c_θ^*	Nondimensional absolute azimuthal velocity	[-]
c_z^*	Nondimensional absolute axial velocity	[-]
c_m^*	Nondimensional absolute meridional velocity	[-]
c_u^*	Nondimensional absolute tangential velocity	[-]
C_τ	Friction velocity: $C_\tau = \frac{\tau_w}{\rho}$	$[\mathrm{m}\cdot\mathrm{s}^{-1}]$
d	Diameter	[m]
D_0	Diameter at inlet of draft tube	[m]
D_1	Diameter at blade leading edge	[m]
D_2	Diameter at blade trailing edge	[m]
D_3	Diameter at guide vane leading edge	[m]
D_4	Diameter at guide vane trailing edge	[m]
D_{ref}	Reference diameter	[m]
E_s	Specific hydraulic energy	$[\mathrm{J}\cdot\mathrm{kg}^{-1}]$
f	Body force	$[\mathrm{m}\cdot\mathrm{s}^{-2}]$
g	Gravitational acceleration	$[\mathrm{m}\cdot\mathrm{s}^{-2}]$
H	Net hydraulic head	[m]
H_l	Hydraulic losses	[m]
H_s	Geodetic suction head	[m]
H_v	Vacuum head	[m]
H_{va}	Vapor pressure head	[m]
k	Turbulent kinetic energy	$[\mathrm{m}^2\cdot\mathrm{s}^{-2}]$
K	Nonspecific constant	[-]
$\dot{m}$	Mass flow rate	$[\mathrm{kg}\cdot\mathrm{s}^{-1}]$
$\vec{n}$	Unit normal vector	[-]
p	Static pressure	[Pa]
p_{atm}	Atmospheric pressure: $p_{atm} \approxeq 0.1\,\mathrm{MPa}$	[Pa]
p_{ref}	Reference static pressure	[Pa]
p_t	Total pressure	[Pa]
P	Unit power	$[\mathrm{kg}\cdot\mathrm{m}^2\cdot\mathrm{s}^{-3}]$
Q	Unit discharge volume flow rate	$[\mathrm{m}^3\cdot\mathrm{s}^{-1}]$
r	Radius	[m]
Re	Reynolds number: $Re = \frac{\rho C L}{\mu}$	[-]
t	Time	[s]
T	Torque	$[\mathrm{kg}\cdot\mathrm{m}^2\cdot\mathrm{s}^{-2}]$
U	Circumferential velocity: $U = r\Omega$	$[\mathrm{m}\cdot\mathrm{s}^{-1}]$
U_{ref}	Reference blade speed	$[\mathrm{m}\cdot\mathrm{s}^{-1}]$
W	Relative velocity	$[\mathrm{m}\cdot\mathrm{s}^{-1}]$
x, y, z	Cartesian coordinates	[m]
y^+	Dimensionless scaled distance: $y^+ = \frac{\rho C_\tau y}{\mu}$	[-]
Z	Geodetic head	[m]

Greek Symbols

α	Angle of incidence, absolute flow angle	[°]
β	Angle of relative velocity vector	[°]
β_B	Angle of blade	[°]
Δp	Pressure difference	[Pa]
$\Delta\eta$	Efficiency diference	[-]
ϵ	Turbulent dissipation rate	$[\mathrm{m}^2\cdot\mathrm{s}^{-3}]$
η	Efficiency	[-]
θ	Angular coordinate	[-]
μ	Dynamic viscosity	$[\mathrm{kg}\cdot\mathrm{m}^{-1}\cdot\mathrm{s}^{-1}]$
ν	Kinematic viscosity	$[\mathrm{m}^2\cdot\mathrm{s}^{-1}]$
π	$\pi = 3.14159$	[-]
ρ	Density	$[\mathrm{kg}\cdot\mathrm{m}^{-3}]$
τ	Shear stress	[Pa]
σ	Cavitation number	[-]
Φ	Flow coefficient	[-]
ψ	Head coefficient	[-]
ω	Radian frequency	$[\mathrm{rad}\cdot\mathrm{s}^{-1}]$
Ω	Shaft (Impeller) rotation frequency	$[\mathrm{rad}\cdot\mathrm{s}^{-1}]$

Subscripts

For variable X,

X_1	Pump inlet location	[-]
X_2	Pump outlet location	[-]
$X_{i,j,k}$	Components of vector	[-]
X_m	Meridional component	[-]
X_{ref}	Reference value	[-]
X_θ	Circumferential component	[-]

Superscripts

$\bar{}$	Average quantity	[-]
$'$	Fluctuating quantity	[-]
*	Nondimensional quantity	[-]
$\rightarrow$	Vector quantity	[-]

Abbreviations and Acronyms

ACE	Area Control Error	
ACG	Automatic Generation Control	
BEP	Best Efficiency Point	
CAD	Computer-aided Design	
CAES	Compressed Air Energy Storage	
CV	Control Volume	
CFD	Computational Fluid Dynamics	
GCI	Grid Convergence Index	
HGL	Hydraulic Grade Line	[m]
MPM	Mixing Plane Model	

MRF Multiple Reference Frame
NPSH Net Positive Suction Head [m]
PDE Partial Differential Equation
PHS Pumped Hydro Storage
PS Pressure Side of blade
PSP Pumped Storage Plant
RPS Renewable Portfolio Standards
RANS Reynolds Averaged Navier-Stokes
RSI Rotor-Stator Interaction
SMM Sliding Mesh Model
SS Suction Side of blade
SST Shear Stress Transport
VAR Volt-Ampres Reactive

Organizations and Agencies

USACE United States Army Corps of Engineers
USBR United States Bureau of Reclamation
TVA Tennessee Valley Authority
NERC North American Electric Reliability Corporation
FERC Federal Energy Regulatory Commission
ORNL Oak Ridge National Laboratory
RTO Regional Transmission Organizations
ISO Independent System Operators
PJM PJM Interconnect
ERCOT Electric Reliability Council of Texas
CAISO California Independent System Operators
WAPA Western Area Power Administration
BPA Bonneville Power Administration
SEPA Southeastern Power Administration
SWPA Southwestern Power Administration

1. Introduction and Background

1.1 Hydropower in the United States

Hydroelectric generation in the United States has been part of the electrical grid generation for over 120 years. The long history of hydropower is evident in the overall age of operational plants. Many of the machines in hydroelectric stations in the United States were commissioned over 30 years ago, and some of the oldest plants have been in operation for over one hundred years. The nameplate capacities of all conventional hydroelectric and pumped storage generators that operated in 2011 are plotted by commissioning year in Figure 1. Even after a long history, hydropower is an integral part of the modern electrical grid and provides significant generating capacity to meet base load demand and balances and regulates loads, among other ancillary services. The need for ancillary services provided by hydropower, such as voltage regulation, has increased in recent years as a greater mix of generation sources have come online. A brief summary of hydropower history and the current state are presented in this section.

Early Years The earliest of the existing turbines was installed in 1891, though many of the older turbines and generators have been upgraded as new technologies and design processes become available. Conventional hydroelectric development grew rapidly in the 1920s. Reversible pump-turbines were first operated in the United States at the Rocky River Plant, Connecticut in 1928. The Rocky River Plant accounted for all new pumped storage capacity in 1928, and was the first of many pumped storage installations in later years. Hydropower development slowed during the Great Depression of the 1930s but rebounded with efforts backed by the federal government. The advent of World War II increased the demand for large quantities of inexpensive electricity to power energy intensive industrial processes such as processing aluminum used to build airplanes. The addition of more hydroelectric generation during these years played an important part in meeting the wartime need for power [1, 2]. This surge of new commissioning between 1940 and 1944 is apparent in Figure 1.

Rapid Growth Hydropower capacity in the United States increased significantly in the later half of the twentieth century. A majority, approximately 65 %, of the current hydroelectric capacity in the United States was installed between the 1950s and 1980s. Development of new hydro projects slowed down after that period of rapid development due in part to high capital costs, increasing environmental concerns, and decreasing availability of suitable sites. The construction of new hydro projects was costly, and investors began backing alternatives such as natural gas fired plants that required lower initial investment. Environmental concerns included water quality, habitat preservation, and fish safety. In addition, many of the most suitable sites for hydroelectric generation already had been developed.

Current State Western states produce most of the conventional hydroelectric generation in the United States. Washington, Oregon, and California produce more than half of the hydropower, as shown in Figure 2. Other states with more than 5 gigawatt hours of installed capacity include South Dakota, Alabama, Arizona, Tennessee, Montana, Idaho, and New York.

In recent years, much of the additional capacity comes from the redesign, replacement, and modernization of existing turbines and generators. Advances in computational tools, e.g., Computational Fluid Dynamics (CFD), provide hydraulic engineers with better performance predictions, resulting in more efficient runner designs. The redesign of outdated runners commonly results in efficiency gains of approximately 1% to 7% in existing

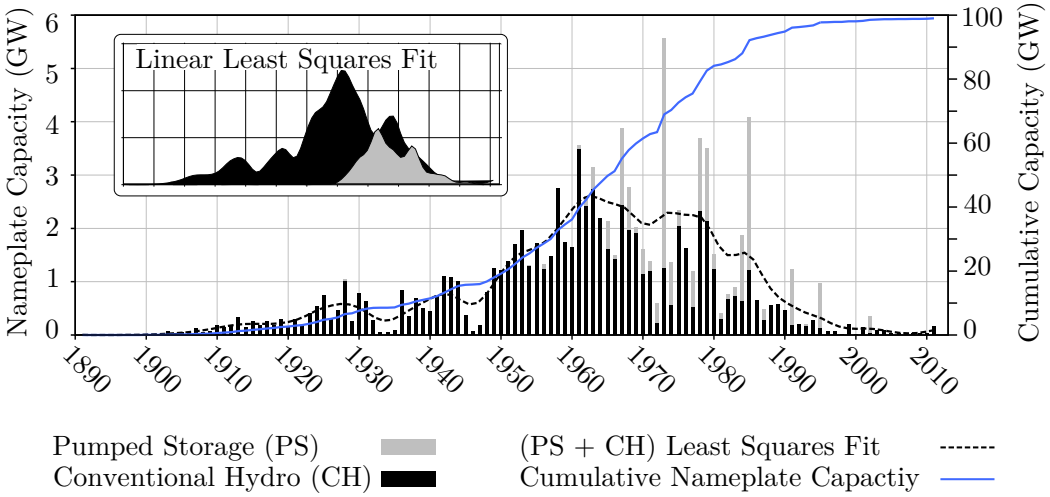

Figure 1. Nameplate capacity of operable hydroelectric generators by the year the unit was first brought onto the grid. Note that the given nameplate capacities may differ from those at initial commissioning because of equipment upgrades. All values reflect capacities of operable units in 2011. The data set excludes units taken out of service for major overhaul or repairs. Data Source: Form EIA-860 (2011), [3].

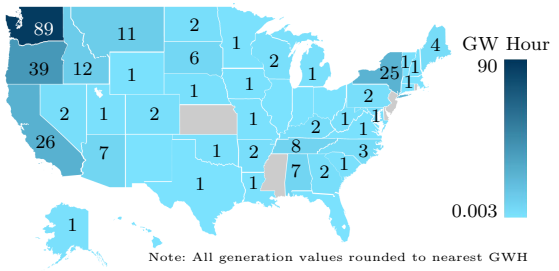

Figure 2. Net Generation of Conventional Hydroelectric by State (2012). Note that all values are rounded to the nearest GW · h. States on the map without numbers generate less than 0.5 GW · h per year. Source: [4].

casings and gains up to 20% with retrofitted water passages, draft tube, and generator [5, 6, 7, 8]. Redesign may include modifications to any part of the hydraulic passage. Commonly modified components are the turbine runner, wicket gates, and stay vanes.

In addition, approximately 3% of the dams in the United States are powered, and efforts are being made to assess the potential of even low-head dams. According to some studies [9, 10, 11], the development of existing non-powered dams could produce an additional 12 GW of hydroelectric power in the United States, a majority of which would come from dams owned by the United States Army Corps of Engineers (USACE).

Plant Ownership The Federal Energy Regulatory Commission (FERC) classifies hydroelectric plants based on whether they are privately or publicly owned. The Federal government owns over 50% of the hydroelectric capacity in the United States [12]. Four federal power administrations market hydropower produced at hydroelectric projects owned by the United States Bureau of Reclamation (USBR) and USACE. The governing agencies transmit and sell electricity from the federal projects. Private utilities own nearly a quarter of hydroelectric generation, and non-federal publicly owned plants contribute approximately 22% of generation in the United States. The remainder of hydroelectric plants are owned by private companies, industry, or cooperatives.

1.2 Integration of Generation Sources

Hydropower is not the only generation source used in the United States. Other common energy sources include natural gas, coal, petroleum, and nuclear. Consider the mix of energy sources used to generate electricity in the United States in 2011 shown in Figure 3. According to 2011 data from the U.S. Energy Information Administration, natural gas and coal powered plants generated 821 144 MW, or over 70 % of total generation in 2011. By comparison, combined generation by hydroelectric and pumped storage accounted for approximately 8.6 % (99 010 MW) of total generation in the same year [13]. Generation from the remaining major non-renewable energy sources, petroleum and nuclear, provided approximately 14.3 % of the total generation. All other forms of generation, including wind and solar, contributed the remaining 5.9 %.

The source of energy largely determines the role of generation in the electrical grid. For example, large nuclear plants usually have relatively low operating costs per MW · h produced and operate continually near maximum power output. This type of plant is called base load generation. These plants have slow ramp rates,

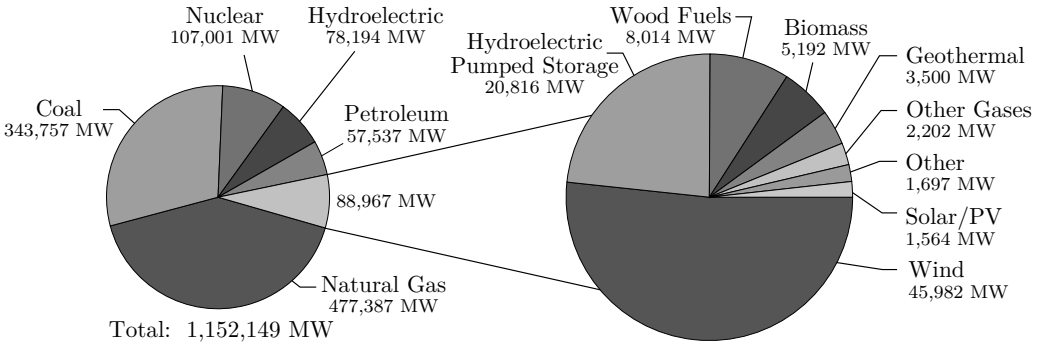

Figure 3. Electric generation energy sources in the United States (2011). Data source: [13].

and changing power output of a large nuclear plant can take days. In contrast to the constant output of base load plants, power output from renewable energy sources such as wind and solar is often unpredictable and intermittent. Consider wind generation. Wind power is the fastest growing renewable energy source in the United States [14, 15]. This growth is notable because wind power has capacity factors of 30 % to 40 %. Power output from wind can fluctuate rapidly and vary hourly or seasonally. Depending upon location, wind turbines generate much of their power overnight when the demand for power is low. This variation in output makes it more difficult to schedule wind resources and requires a level of capacity firming. Other generation sources and energy storage are needed to smooth these variations in power output and to follow real-time loads.

Energy storage is an essential tool used to maintain a balanced electrical grid and can reduce the effects of intermittent generation from renewable sources. Utility-scale energy storage provides a unique service because it can both consume and supply energy. Historically, energy storage has been used to time-shift electrical power to improve the efficiency of base load plants [16]. Energy time-shifting can occur over minutes, days, or even months in the case of seasonal variation. In addition to time-shifting power, energy storage can help alleviate transmission congestion and improve grid stability by providing backup capacity, reactive power, regulatory functions, and ancillary service such as frequency and voltage control.

Renewable Energy Time-shifting Renewable energy sources are capable of matching loads on a minute-to-minute or hourly basis, but generation can be intermittent and redundant generation capacity or energy storage is needed to ensure that real-time loads are met. Photovoltaic cells produce electricity only when the sun shines, and solar generation peaks around mid-day. This generation profile matches typical load trends exhibited in Figure 4. The figure shows average hourly loads from the Mid-Atlantic Region of the PJM Interconnect. Note the peak demands in the afternoon hours and low demand overnight. Demand for electricity is also greatest during the summer months when the use of air conditioning is common.

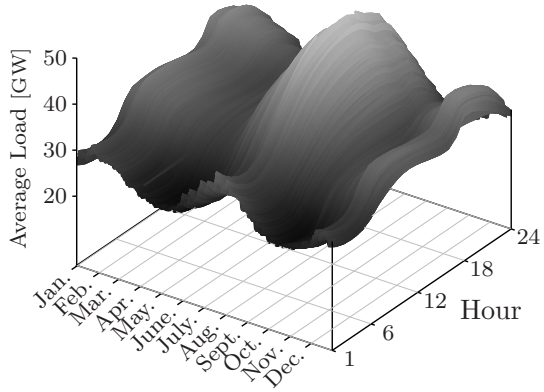

Figure 4. Typical daily variation of grid load over a year. Note the peak demand in the afternoon hours and low demand overnight. This figure uses hourly loads averaged over 11 years from the PJM Interconnect Mid-Atlantic Region (January 2002 to July 2013). Data source: [17].

However, maximum power output from solar may not necessarily coincide with times of highest demand. Solar power is treated as must-take generation and if energy storage is not available, other energy sources must compensate by ramping production down in morning hours and ramping back up in evening hours as solar output decreases. When paired with solar output, wind generation can help smooth power output because wind generation is typically highest overnight. Electric energy time-shifting helps avoid the need for demanding ramp rates and additional energy procurement or curtailment by storing excess energy for later use.

Renewable Capacity Firming Renewable capacity firming refers to dispatchable generation needed to back up intermittent and variable wind and solar generation for a period of time. Stored energy is used to meet ramping demands created by solar and wind overproduction or

underproduction and prevent fluctuations in grid power and voltage while maintaining desired level of generation. These ramp rates can be on the order of several $\mathrm{MW} \cdot \mathrm{min}^{-1}$, thus requiring that significant resources be committed to a reserver margin as either spinning or non-spinning reserves. Any units designated as reserve do not generate at full power, if at all, and lower the maximum power output a plant from a market perspective. Overgeneraton occurs at times of unexpected low load or at times when dispatchable generation has been curtailed and must-take generation that is kept online exceeds current demand for electricity. Excess energy must be absorbed or transmitted to another region when available downward load-following resources are unavailable or have been exhausted. If sufficient energy storage is not available and regional transmission of excess energy is not possible, the real-time energy prices may become negative.

Methods of Energy Storage Many methods are capable of storing electrical energy, though few methods are commercially viable for bulk energy storage at the grid level. Power capacity and discharge duration are two of the most important criteria when assessing energy storage. Pumped storage is currently the only available large-capacity dispatchable resource capable of rapid response and absorbing or providing hundreds of $\mathrm{MW} \cdot \mathrm{h}$ of power. By some estimates, pumped hydro storage accounts for approximately 98 % of the installed energy storage capacity worldwide [18]. Figure 5 shows the global installed capacities (2010) of other common energy storage methods.

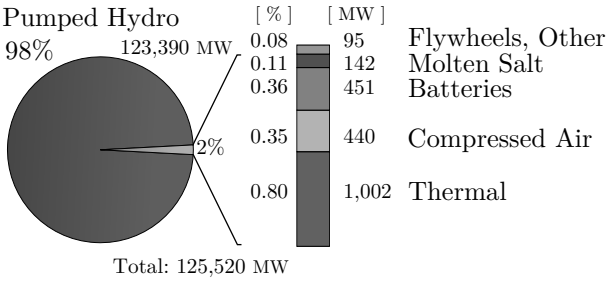

Figure 5. Estimated global installed energy storage capacity by technology (2010). The estimate shown here only includes thermal energy storage for cooling. Source: [18].

Batteries and flywheels are two common types of energy storage used to provide grid services. Batteries store electrical energy in chemical form and have limited capacity and cycle life. The power rating of batteries varies from a few kW to several MW. Large-capacity batteries are capable of providing grid support such as load shifting up to several $\mathrm{MW} \cdot \mathrm{h}$ of power. Many types of batteries also can improve power quality and stabilize grid frequency. Like batteries, flywheels can be used in frequency control and regulation applications. However, flywheels store kinetic energy as angular momentum in a spinning rotor that is attached to a motor/generator. To store energy, the motor spins the rotor at high speeds, often at rates of 10 000 rpm to 20 000 rpm. When power is needed, the motor becomes a generator and energy is recovered. Flywheels have rapid cycle times and can be quickly cycled between modes because the rotor spins in the same direction in storage and generating modes. A single flywheel usually has a power rating under 1 MW, often in the range of 100 kW to 1650 kW. Flywheels are limited in size and therefore have a low energy density, making them most suited for meeting short-term energy demands. Flywheels are not suited for bulk energy management or sustained load shifting.

Compressed air energy storage (CAES) and pumped hydro storage are the only commercialized bulk energy storage technology in the United States. CAES systems store electrical energy by filling large tanks or underground caverns with compressed air. When power is needed, air is released from the reservoir to spin a turbine. Before passing through the turbine, the air may be heated as it expands to improve efficiency. Capacities range from 3 MW to 50 MW for small above ground plants and up to 400 MW for large underground storage. Sustained discharge time for CAES systems is usually several minutes, up to an hour.

1.3 Pumped Storage

Pumped hydro storage (PHS) is by far the most common form of bulk electrical energy storage in the United States and accounted for 98.6 % of installed storage capacity in 2012 [19]. Pumped storage is the only technology capable of rapid response, ramp rates on the order of $\mathrm{MW} \cdot \mathrm{min}^{-1}$, and sustained discharge or storage for hours. In addition, the rated power capacity of PHS can be approximately 10 times larger than compressed air and 100 times the capacity of most batteries.

Pump-turbines pump water through a penstock to an elevated reservoir to be released at a later time. A typical pumped storage plant layout is shown in Figure 6. Another arrangement is a closed loop system with the lower reservoir located underground in an abandoned mine or natural cavern. The location of PHS plants is almost entirely based on geography due to the need for an upper and lower reservoir and proximity to a water. The difference in elevation between the upper and lower reservoirs can vary from a few meters to over 1500 m. Required pump head over 700 m usually require multi-stage pumps and impulse turbines.

The first hydroelectric pumped storage plant in the United States, the Rocky River Plant in Connecticut, uses reversible pump-turbines and began operation in 1929. Over time, hydro turbines and pump-turbines have increased in physical size and rated capacity. Larger turbines typically are more efficient because secondary

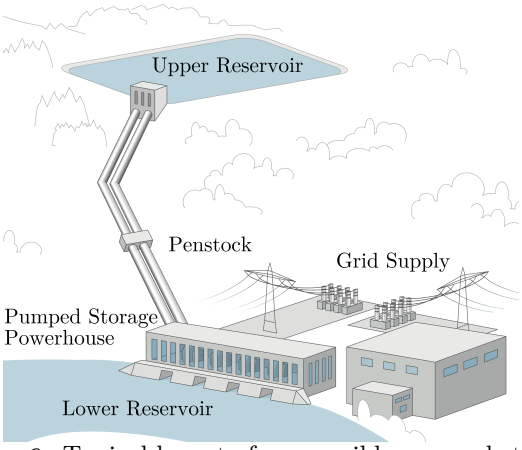

Figure 6. Typical layout of a reversible pumped storage power plant. Adapated from source: [20].

losses, such as viscous losses and leakage between seals, account for a smaller percentage of the total power.

Pumped storage is considered a mature technology and is uniquely suited to meet the growing need for electrical power regulation by absorbing bulk quantities of excess power and providing discharge times of 8 to 10 hours at cycle efficiencies of approximately 76 % to 85 %. Figure 7 shows energy flow through a single round-trip cycle through a pumped storage plant. Power losses from transformer, motor/generator, and shaft lines are relatively small compared to the combined hydraulic losses in the draft tube, impeller, and penstock.

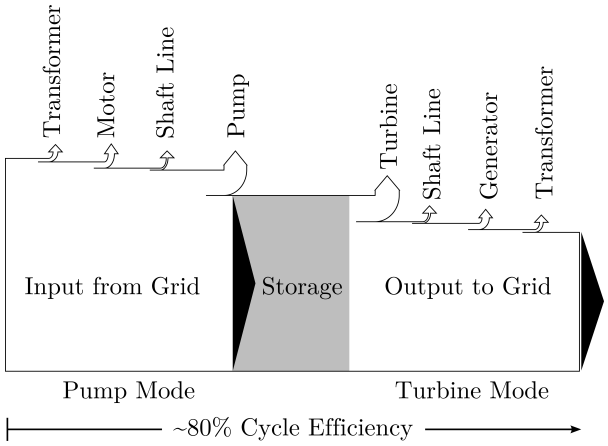

Figure 7. Example energy flow for a single round-trip pumped storage cycle. Cycle efficiencies around 80 % are common. Adapated from source: [21].

Common pump-turbines used in pumped storage applications include:

1. Synchronous single speed reversible pump-turbine
2. Variable speed reversible pump-turbine
3. Ternary set of pump and turbine
4. Deriaz pump-turbine with adjustable blades

Synchronous single speed reversible Francis pump-turbines are the most common in the United States. Variable speed turbines are increasingly common because of recent advances in power electronics and increased need for ancillary services and flexibility. Ternary sets typically consist of a separate pump and turbine linked through a common motor-generator. Ternary pump and turbine sets provide operation over a wide range of heads and power through hydraulic short circuits where all or part of the discharge from one hydro machine is fed directly into the other machine. Deriaz pump-turbines operate at low heads and use adjustable blades for optimal performance. This thesis addresses operating conditions in synchronous single speed Francis machines.

1.4 Services Provided by Pumped Storage

Pumped storage historically provided peaking power to improve efficiencies of thermal base load generation. Current uses of pumped storage include peaking capacity, bulk energy storage, and ancillary grid services. Power grid operators generate revenue through energy arbitrage and ancillary services such as voltage control, frequency regulation, and firming capacity. Like conventional hydro, pump-turbines in spinning reserve mode can go from zero load to full load within seconds and serve dispatchable assets. Common ancillary services include operating reserves, voltage support, frequency regulation, and black start service.

1.4.1 Grid Support and Power Quality

Reserve Capacity Scheduled reserve capacity can be online or offline and typically has the capacity of approximately 15 % to 20 % of total grid capacity. Offline reserve capacity is known as non-spinning reserve. Spinning reserves are defined as machines under no load that are online, synchronized with the grid, and ready to generate electricity immediately. Spinning reserves do not provide energy to the grid until called upon to balance loads and can be deployed within 10 minutes in response to signals from an Automatic Generation Control (AGC) system. Rapid-response spinning reserves used for frequency control can respond within 10 seconds. Non-spinning reserves are offline generating units or loads that can be curtailed or brought online quickly, usually within 30 minutes.

Voltage Support Energy storage also provides backup power needed to maintain voltage levels on the electrical grid, usually within 5 % of target voltages. This service compensates for voltage sag and unstable voltage due to disturbances caused by events such as a generator fault or unexpected load shedding. Reactive power support is the primary method used to maintain voltage levels. Generators produce reactive power to overcome reactance

in the grid and provide reactive power to inductive loads such as transformers and synchronous motors. Voltage can vary throughout a system based on line loads and local reactive power levels. Therefore, generator volt-ampere reactive (VAR) capacity and location on the grid is important for voltage regulation. Synchronous generators with variable excitation control are the main sources of reactive power. Pump-storage systems may provide VAR support while supplying real power, storing energy, and even without supplying or consuming energy while acting as spinning reserves. At least 30 minutes of voltage support is usually needed to stabilize the grid.

Regulation and Frequency Response Regulation meets fluctuating loads on a second-to-minute basis while frequency response occurs within seconds. In the context of an energy storage system, energy is released (regulation up) and power is generated to correct negative imbalances between supply and demand. Conversely, consumption of electrical energy from the grid, either to be stored or as an added load, is known as regulation down. The cost of regulation services is directly affected by storage cycle efficiencies.

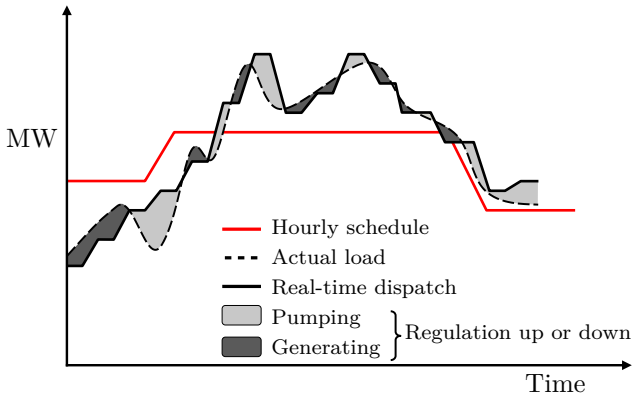

Figure 8. Load regulation meets fluctuating loads on a second-to-minute basis. Adapted from source: [22].

Grid frequency is continuously monitored and adjusted to maintain system-wide frequency standards set by the North American Electric Reliability Corporation (NERC). Grid frequency, 60 Hz in the United States, dictates the speed of synchronous generators. For example, a drop in grid frequency due to a turbine failure is reflected in a change in generator speed of other units. Generator governors on conventional hydro turbines and pump-turbines monitor the generator speed. If a change in speed is detected, the unit automatically responds by opening or closing the wicket gates to adjust power and effectively stabilize the grid frequency. These adjustments are sensitive and take place automatically and occur within 10 to 20 seconds. In addition to this automatic frequency response, a central balancing authority monitors frequency on the regional grid and flow through interconnects. The balancing authority sends AGC signals to plants on a minute-to-minute basis to maintain grid frequency by deploying spinning and non-spinning reserves.

Load Following Load following generation is the capacity difference between the hourly, day-ahead schedule and the real-time dispatch needed to match an actual load as shown in Figure 9. Load following is achieved by adjusting power output or by managing loads on a 5 min to 10 min basis to compensate for differences in electrical supply and demand, and it sometimes results in severe ramp-rate requirements. Pumped storage systems perform well as load following generation because they offer rapid response and are capable of load following up and load following down. Load following up occurs in cases where short-term scheduling underpredicts demand and generator output increases to meet the real-time load. In the inverse scenario, generation is turned down to match a decrease in demand. This is known as load following down. Negative energy prices can occur if power producers continue generating despite a decrease in demand. Non-dispatchable resources commonly used in base load generation, such as nuclear stations, often have long start-up and shut-down lead times. So, it remains profitable to continue to generate electricity even though the producers essentially pay to generate. Generators designated for load following may operate below rated capacity when loads increase. Part load operation away from the design point is often costly in terms of lower efficiencies and equipment degradation.

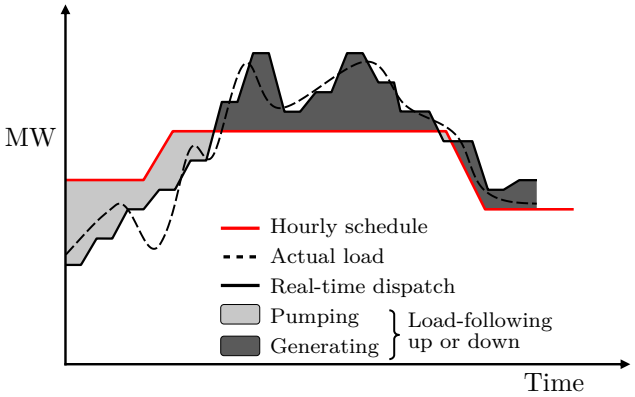

Figure 9. Load following compensates for differences in electrical supply and demand on 5 min to 10 min intervals. Adapted from source: [22].

In addition to adjusting generator output, system load can be used to balance supply and demand. One way to affect system loads is to increase or decrease pump input power at pumped storage plants. The development of adjustable speed pump-turbines allows operators to decouple motor speed from grid frequency and make adjustments in load over a wide range of powers. However,

many adjustable speed units are limited in size and are more expensive compared to conventional synchronous pump-turbines.

In the absence of extreme circumstances, regulation capacity is always less than load-following capacity. For example, the average required regulation up capacity over all hours of a day in 2011 in the California Independent System Operators (CAISO) service area was approximately 41 % of required capacity for load following up. The CAISO service area covers approximately 80 % of California and a part of Nevada. Over the same time, the average required regulation down capacity was similarly 42 % of required capacity for load following down. Load following and regulation capacities are a measure of the amount of variability on the grid and are therefore seasonally dependent. In the CAISO scenario, the need for load following capacity is greatest during summer and fall months and lowest in the winter and spring [22].

Black Start Capacity Black start capability provides the necessary generation, usually around 5 MW to 50 MW, to reestablish a stable grid in the event of widespread outages. Energy storage can provide generators to come back online after an outage without using electricity from the wider grid. In hydro plants, diesel engines or other power sources are used for generator excitation. The quantity of stored energy at pumped-storage projects is usually capable of supplying sufficient power to bring other generators online.

1.4.2 Energy Management

Load Shifting and Arbitrage Traditionally, pumped storage was used for energy balance and time-shifting energy arbitrage based on the differential in energy prices at storage and generation. Electrical power was consumed by pumping water at times of low demand, usually during the night, and released to generate electricity during times of higher demand during the day. An example of this type of pumped storage scheduling is shown in Figure 10. This figure displays average of 10 years of combined data from generators at the Grand Coulee Dam. Pumping power consumption data are from the 12 pumps at the Grand Coulee pumping station averaged over several weeks. The figure clearly shows that peak generation occurs in the morning between hours 8 to 11 and again in the evening between hours 18 to 22. Generation is lowest and energy storage through pumping is greatest overnight when demand is low.

This load shifting is known as energy arbitrage when revenue is generated from the differential in prices at the time of energy storage and generation. The energy at off-peak hours is less expensive than that at peak demand, and the difference in price accounts for the profits of energy arbitrage. The profitability of this type of service is highly dependent on energy prices and round trip

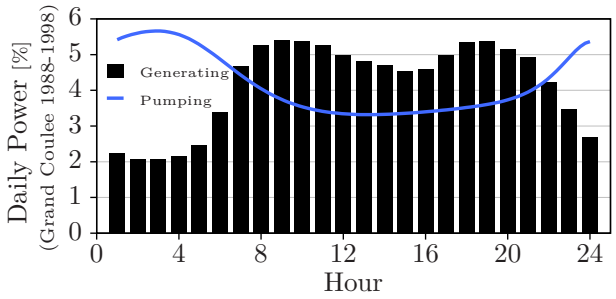

Figure 10. Typical hourly hydroelectric generation and pumping over a day. Generating data are from all generators at Grand Coulee Dam and are averages from 1988-1998. Pumping power consumption data are from the 12 pumps at the Grand Coulee project averaged over several weeks in the summer. Data source: [23, 24].

efficiency of storage plants. Frequent changes between generation and storage are common to take advantage of spot-market prices. Studies suggest that energy arbitrage by itself is not profitable enough to recover capital costs of new energy storage plants [25, 26, 27]. Other services, such as frequency control, must be monetized as well.

Supply Capacity Supply capacity is simply reserve capacity that can be used as needed. Though not true arbitrage, electricity supply capacity is included in this category because it fills gaps in generation schedules and can diminish the need for additional generation plants or procurement of electricity at times of high demand. Supply capacity may meet daily peaking loads or be sold as base load generation in the wholesale markets. Supplied capacity from storage is typically provided for a few hours at a time.

2. Motivation and Overview of Study

2.1 Motivation

Since the introduction of reversible pump-turbines in 1928, Francis pump-turbines have become the most common machine used for hydro pumped storage in the United States. Pumped storage provides generation and ancillary services to electrical grids because of its high power density and flexible generation characteristics. Operating pump-turbines over a wide range of flows is desirable because it allows for greater grid stabilization and has recently become more important because of increased penetration of intermittent generation sources such as wind and solar.

Increasing amounts of intermittent generation, such as solar and wind, are being added to energy portfolios. The push for more renewable energy in the United States is reflected by state and federal Renewable Portfolio Standards (RPS) that mandate increased levels of renewable generation. RPS regulations vary by state, but they often require increased production of solar and

wind power to meet a set percentage of total capacity. Goals for renewable energy production range from 10 % of generation in several states up to 40 % of generation in Hawaii by 2030 [28]. Compliance is voluntary for some goals, while other regulations are enforced with penalties.

The increased penetration of wind and solar generation contributes system-wide variability because these resources are difficult to accurately forecast and reliably dispatch. Wind and solar production fluctuates seasonally and varies on a short enough timescale to affect five-minute dispatch scheduling. Improved day-ahead wind forecasting can improve plant capacity factors and reduce the impact of renewable penetration on the stability of regional power grids. However, advanced forecasting techniques and new technology have not eliminated uncertainty. The stochastic nature of these energy sources increases the need for grid regulation and capacity firming provided by high capacity and rapid-response energy storage.

Pump storage plants help integrate renewable generation sources into the grid by providing regulation, load shifting, and capacity firming. In addition to absorbing excess energy from over-generation and providing peaking power, pumped storage helps smooth variability due to intermittent generation and helps improve power quality.

Voltage stabilization can be achieved through reactive power management in both generating and pumping modes by adjusting motor-generator excitation. Variable speed pump-turbines use power electronics to vary the frequency supplied to the rotor windings, causing a phase shift between the magnetic fields in the stator and rotor. This phase shift between the stator and rotor currents will either consume or supply reactive power and can be used to change the speed of the pump impeller.

The rotational speed of synchronous pump-turbines that are connected to the grid is set by the line frequency and number of poles in the motor-generator. Direct current is sent to the rotor windings, and the rotor speed matches the rotating magnetic field created by the alternating current in the generator stator. The pumping power of a Francis pump-turbine at a single impeller speed is based on the required head and discharge. A single performance curve specifies all available operating point for the synchronous speed pump at a given head. The useful operating range is bounded by cavitation limits.

Other considerations include the required head range in pumping mode. The maximum head achievable in pumping mode may not match the conditions for best efficiency in generating mode. The so-called “S-shaped" instability in the head curve at low discharge must also be avoided, especially for high specific speed pumps. Therefore, the design of single speed Francis pump-turbines is a compromise between the optimal designs for centrifugal pumps and Francis turbines. From the perspective of the head change across a synchronous, reversible pump-turbine runner, the maximum net head reached in pumping mode usually will be lower than the maximum useful head of the turbine in generating mode. This is the case because pump power must overcome hydraulic losses in the penstock. Therefore, reversible pump-turbine design often favors pump operation and results in non-optimal generation.

Variable Power Traditional Francis pump-turbines are single-speed machines that operate on a performance curve determined by a one-to-one correlation between head and capacity. Advances in power electronics have made it possible to decouple the speed of large pumps from the grid frequency with variable speed motor/generators. Variable power consumption is desirable because it helps plant operators maintain tighter control over regulation and load-following. The dispatch of pumps and turbines results in discrete step changes in power consumption or generation. Therefore, not all loads can be exactly matched to the potential of every unit in a plant. For example, consider a plant with three identical pump-turbines that each have a capacity of 50 MW at the best efficiency point (BEP). A net sink or source of 50, 100, and 150 megawatts of output power can occur if each unit is operated at BEP. In practice, greater flexibility in power levels is available by operating at off design conditions and by using units in parallel with a combination of some units pumping and other units generating. Still, gaps in optimal scheduling can occur.

The introduction of variable speed pump turbines improves flexibility. Near continuous variation in power levels can be achieved with variable speed pumps by decoupling the rotor frequency from the grid frequency as discussed previously. Affinity laws, derived from the dimensional analysis of pump design parameters, show that the change in pump power between two identically sized impellers pumping the same fluid is proportional to the cube of the speed ratios. For example, a 10 % reduction in speed will require approximately 73 % of the power needed at the original speed. Changing the rotation speed can increase the efficiency at partial loads. Variable speed pumps operate over a range described by a hill chart similar to the one used in turbine mode and can increase the usefulness of pumped storage [29]. However, variable speed units are costly and have limited capacities.

2.2 Proposed Idea: Pre-Whirl Control

The goal of this research is to investigate whether pre-whirl can be used to improve off-design operation of a synchronous pump by a) increasing efficiency by reducing internal losses, b) providing variable power storage by controlling torque, and c) expanding the operating range by suppressing the onset of recirculation at low flow

operation.

The goal of the present research is to shift the operating curve of synchronous machines to optimize performance at off-design conditions and regulate power in pumping mode. The idea is to regulate pumping power synchronous units by adjusting operating parameters on the pump rather than varying speed by decoupling from the electrical grid frequency. The pump could rotate at a single synchronous speed, but the input power could increase or decrease at a given head. The operating characteristics of a pump at off design conditions, especially at low flow rates, could be adjusted in real time with active controls such as inlet guide vanes or inlet swirl blowing intensity.

Modifying flow characteristics is another approach to regulating power and achieving a larger operating envelope in pumping mode, and researchers have shown that introducing pre-whirl can improve efficiency in compressors and small pumps. Adding pre-whirl in the direction of impeller rotation improves efficiencies at lower flows. Adding reverse whirl improves efficiency at higher flows. It should be noted that the small pumps studied have a BEP efficiency of only approximately 80 %. Hydraulic losses in larger pumped-storage units are a smaller percent of the total power, and BEP efficiencies are well into the 90% range.

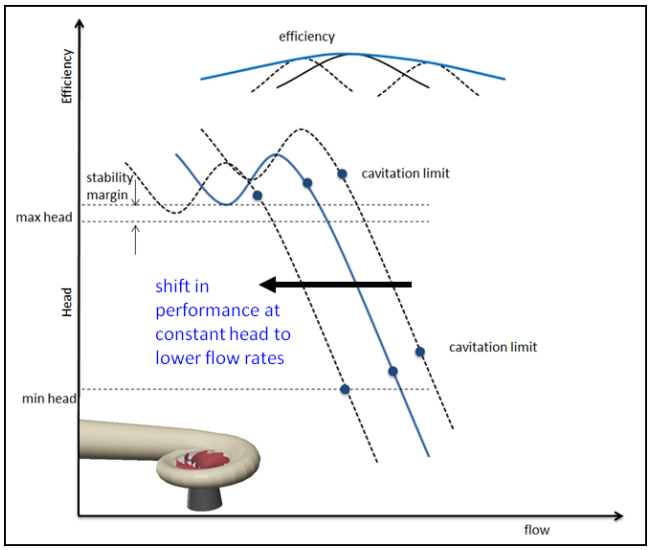

Figure 11. Greater flexibility in power regulation can be achieved by improving the performance at off-design operation.

Flow straighteners and inlet guide vanes can modify flow behavior and have been shown to improve efficiency at off design operation of compressors and centrifugal pumps [30, 31, 32, 33]. For example, Tan [30] demonstrated that positive pre-whirl induced by three dimensional guide vanes at part load operation in a centrifugal pump reduced reverse flow and improve efficiency by up to two percent. In these studies, reverse flow appears near the walls as the flow rate drops. Ideally, the axial flow should be uniform at the inlet. The goal of the present research is to improve the incident angle, and thus control the onset of recirculation by providing some pre-whirl at low flows to adjust the velocity distribution upstream of the impeller.

The following options are available to regulate power of synchronous pump-turbines.

I. Variable power consumption at a set operating point by adjusting power at a head and flow rate of a specific operating point. This can be achieved in one of two ways

   a Consume more power by adding an additional load or internal hydraulic losses. Adding losses consumes power, but decreases the machine efficiency.
   b Reduce hydraulic losses in the flow passage. This will improve efficiency, but may cause unfavorable flow conditions that are only acceptable for short operating time.

II. Reduce hydraulic losses at off-design flow conditions. Use the off-design operating parameters as a design point and modify flow through the pump to optimize performance. This creates a new power curve and improves efficiency at low flow.

III. Extend the limit of stable operation at part-load operation to lower flow rates. This often requires modification to the flow passage or impeller.

2.3 Study Overview

The objective of the present work is to investigate the effects of pre-whirl on pump performance. In the current study, pre-whirl is induced by adding blowing of water through openings in the draft tube cone. The blowing angle allows for active control and the option of influencing the flow only at off-design conditions. The inlet suction cone accelerates the flow and improves the uniformity of the velocity distribution and fluid turbulence entering the pump.

Computational Fluid Dynamics (CFD) is used to predict performance and stage losses in a pump. A case study is used to investigate the effects of pre-whirl on pump performance. The pump used in this study is from the pumping station at the Grand Coulee Dam, shown in Figure 12. The pump has nine impeller blades and fixed distributor vanes in the spiral case. After an initial analysis of steady-state flow through a single periodic blade passage, the computational domain was expanded to include the draft tube, complete pump impeller, and spiral case. Moving mesh simulations were completed in ANSYS® Fluent. A $k-\omega$ SST turbulence model is applied to a fully structured grid of nearly 11 million cells.

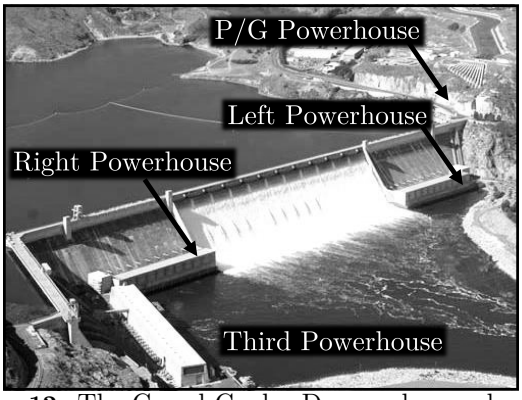

Figure 12. The Grand Coulee Dam and powerhouses are located on the Columbia River. The Grand Coulee project consists of the dam and Left, Right, Third, and Pump-Generating powerhouses. The Left and Right powerhouses were constructed between 1933 and 1941. Pumping operations for irrigation began in 1951. The Third powerhouse was added later (1967-1974), and the last turbines were installed by 1980. Many of the dams on the Columbia River are owned and operated by the U.S. Army Corps of Engineers and U.S. Bureau of Reclamation. Adapted from source: [34].

3. Pump Theory of Operation

Hydro turbomachines are classified by the method of energy exchange. Turbine design depends on the available head and flow rate. Common operating ranges of head and discharge for various machines are shown in Figure 13. Pelton turbines are typically operated at heads higher than 200 m and, are used nearly exclusively for heads above 700 m. In contrast, bulb turbines perform well at heads below 20 m and relatively high flow rates. Conventional single stage Francis, Kaplan, turbines and reversible pump-turbines perform well at head ranges between those of Pelton and bulb-type turbines. Pump-turbines combine the qualities of Francis turbines and centrifugal pumps and are usually single stage. Low specific speed pump-turbines differ little from Francis turbines. The runner diameter and exit passage area dimensions of Francis turbines depend on specific speed for the design. In some cases, multi-stage pump-turbines are used for high head applications.

The interdependence of discharge, Q, and head, H for each class of turbomachine can be summarized by a single dimensionless quantity, called specific speed. Several definitions of specific speed are used in practice, but in general, low specific speeds are characterized by small flow rates and high operating heads. Conversely, high specific speed pumps operate at lower heads and higher flow rates. The definition of specific speed, ν_s, used in this paper is given in Equation 22. The machine investigated in this paper is a single stage, reversible pump-turbine and has a specific speed of $\nu_s = 0.27$.

3.1 Description of Components

Reversible pump-turbines are coupled with a generator-motor and are capable of both generating power in turbine mode and consuming power in pumping mode. In generating mode, the penstock delivers water from an upper reservoir to the turbine. Water flows from the penstock and through a spiral case, past guide vanes, through a turbine runner, and exits via a draft tube. In pumping mode, the rotation of pump-turbine and direction of flow is reversed. The generator acts as a motor and supplies power to the pump-turbine.

A typical hydroelectric powerhouse layout includes a row of turbines similar to the one shown in Figure 14. The most common orientation of the turbine axis of rotation is vertical. The turbine shaft attaches to a generator, most often located above the turbine in a de-watered pit, through a vertical main shaft. The spiral case, runner, and draft tube are completely filled with water. The submerged runner and the generator pit are separated by a head cover. The head cover also supports a bearing and seal around the main shaft.

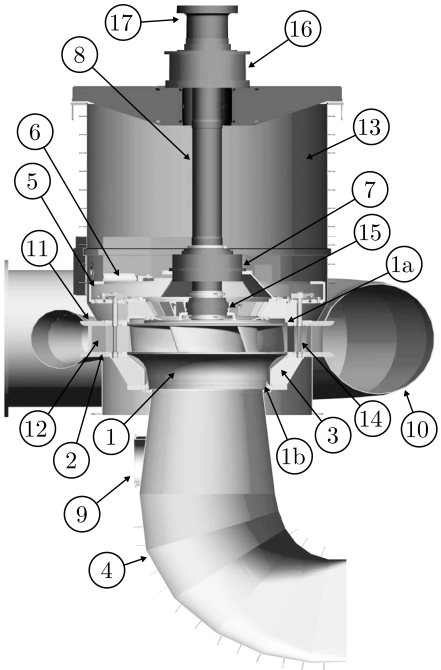

Figure 14. Reversible Francis Pump-turbine. Names of numbered parts are located in Table 1. Adapted from source: [36].

Hydraulic performance of a pump-turbine is largely determined by the design of four components: the spiral case, guide vanes, runner, and draft tube. Each of these components can be found in the labeled diagram of a vertical shaft, reversible Francis pump-turbine that is displayed in Figure 14 and listed in Table 1. A short description and the purpose of each component is discussed here.

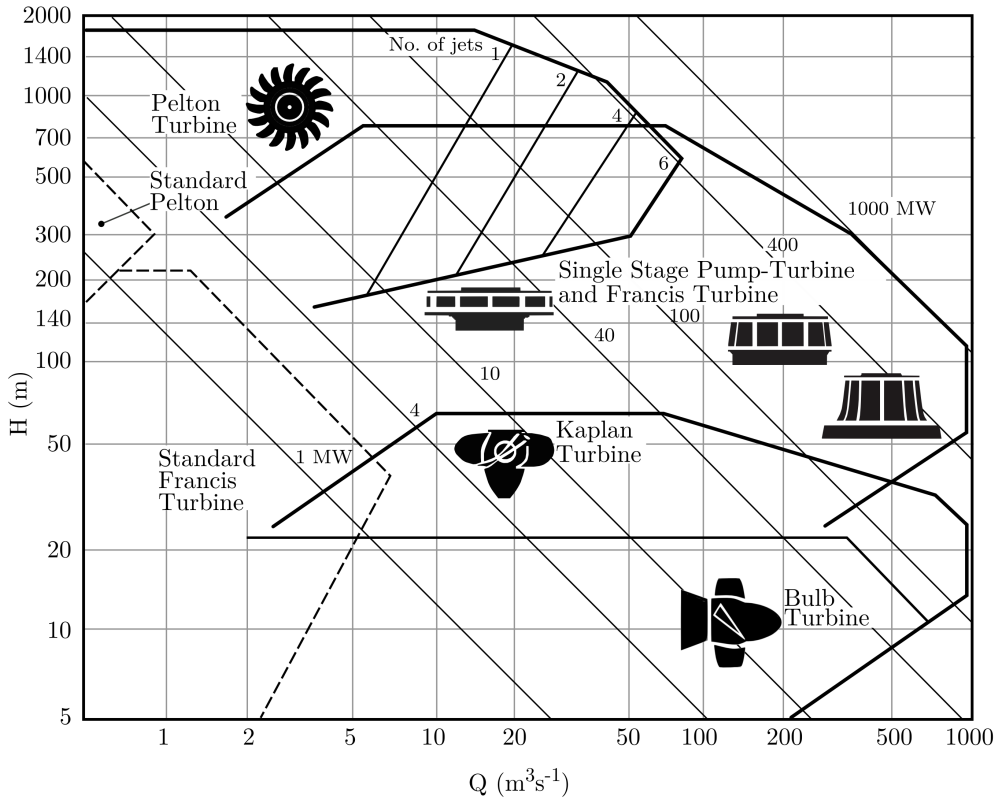

Figure 13. Head and flowrate ranges for various hydraulic turbines. Lines of constant power are shown. Adapted from source: [35].

Table 1. Francis and Pump-Turbine Nomenclature. Numbers correspond with labeled components in Figure 14.

No.	Description	No.	Description
1	Runner	9	Man Door
1a	Runner Crown Seal	10	Spiral Case
1b	Runner Band Seal	11	Stay Ring
2	Bottom Ring	12	Stay Vanes
3	Discharge Ring	13	Turbine Pit
4	Draft Tube	14	Wicket Gates
5	Gate Operating Ring	15	Main Shaft Seal
6	Gate Servomotors	16	Thrust Bearing
7	Main Guide Bearing	17	Coupling Flange
8	Main Shaft		

Spiral Case The purpose of a spiral case and distributor assembly in generating mode is to uniformly direct incoming flow onto the leading edge of the turbine runner and maintain constant angular momentum. The spiral casing is shaped with decreasing cross-sectional area to maintain equal inlet velocities as the flow rate decreases around the turbine. Spiral cases may be constructed from welded steel sections or formed directly by pouring concrete around a form. For added strength, steel draft tubes may be encased in concrete.

In pumping mode, the spiral case acts as diffuser and aids in pressure recovery. Velocity slows and kinetic energy is converted into increased pressure, raising the apparent head produced by the pump. Hydraulic losses in the spiral case can be significant, and they must not be neglected when evaluating efficiency.

Guide Vanes Guide vanes can be fixed in position, as in the case of stay vanes, or may be adjustable. Fixed stay vanes in the distributor direct flow from the spiral case onto adjustable wicket gates. Alignment of flow with the wicket gates reduces turbulence and hydraulic losses. In addition to guiding flow, stay vanes provide structural support in the spiral case and connect the upper and lower sections of the spiral casing.

Movable wicket gates are located between the ring of stay vanes and the turbine. An operating ring links the

wicket gates so they move simultaneously. Servomotors actuate the operating ring to adjust the wicket gate position and regulate the flow through the turbine and thus the power output of the turbine. Flow is redirected by the wicket gates as it enters the runner. Wicket gates can be opened or closed to change the direction (swirl) and the volume flow rate (power) provided to the turbine. Inlet swirl is adjusted so flow enters the runner at a slight angle of incident with the leading edge of the rotating blade at the best efficiency point (BEP).

Runner A runner is the most important component in determining performance characteristics. A runner is constructed of curved blades fixed to a hub, often referred to as a crown, and an outer band. The band strengthens the runner and allows for thinner blades, and thus lower flow blockage through the blade passage. The crown attaches to a main shaft that transmits power to a generator. Turbine runners typically have 12 to 18 blades and some may have blunt trailing edges. Francis pump-turbines differ little from low specific speed turbines and usually have 6 to 9 blades. Bi-directional flow in pump-turbines necessitates rounded edges on both the leading and trailing edges of blades. Components may be cast, machined, or formed from materials such as cast iron or stainless steel.

The runner is completely submerged, and pressure throughout the runner is above atmospheric pressure. The effective head across the turbine is a measure of the hydraulic energy of the machine. Curved blades redirect and change the angular momentum of flow as it passes through the runner. This change in angular momentum is accompanied by a change in pressure and kinetic energy. Changes in kinetic energy can take the form of changes in fluid speed or mechanical torque of the runner as it rotates.

Draft Tube The draft tube is located between the runner and tailrace. In generating mode, water passes from the runner, through the draft tube, and is discharged into a tail race. The tail race is a body of water with a free surface at atmospheric pressure (standard atmospheric pressure at sea level is 101 325 Pa, but varies with location). In pumping mode, the draft tube supplies water to the pump. Like the spiral case, draft tubes usually are constructed from welded steel sections encased in concrete for strength.

The primary function of the draft tube is pressure recovery. The draft tube acts as a diffuser and recovers kinetic energy from the flow by decreasing velocity and converting it to potential energy in the form of increased pressure. Pressure recovery in draft tubes allows the pressure of the fluid exiting the runner to be lower, increasing the net pressure difference between the runner inlet and outlet. A larger pressure difference between runner inlet and outlet improves the power and efficiency of the turbine at a given discharge.

An elbow draft tube consists of three sections, each with a specific function. A cone connected to the runner outlet slows the flow and recovers pressure. A turn in the flow passage, the elbow, changes the flow direction by an angle of approximately 90 degrees (vertical to horizontal). Flow through the elbow often produces additional losses caused by flow separation or other secondary flows. Accelerating flow through the elbow can improve flow conditions and reduce losses. An ideal draft tube would not have this elbow, but it is often present for practical reasons so that an appropriate turbine setting can be achieved with minimal excavation. Finally, another diffusing section decelerates the flow again and directs flow into a tailrace.

3.2 Working Principle

Fundamentally, centrifugal pumps transfer energy to a working fluid in a manner consistent with the laws of motion and thermodynamics. That is, the total mass, energy, and momentum of the system are conserved as changes in fluid velocity, static pressure, and temperature. A motor applies torque to an impeller and causes it to rotate. Impeller blades impart energy to the fluid and increase fluid velocity and static pressure. Viewed from an absolute reference frame, impeller blades force fluid radially outward along a curved path. Centripetal acceleration ($r\omega^2$) opposes the centrifugal acceleration of the fluid through blade passages. Centripetal forces appear in the fluid as a positive gradient of static pressure in the radial direction. The difference in total pressure between the outlet and inlet of the pump is a measure of useful energy added to the fluid. The hydraulic efficiency of the impeller is the proportion of input power from the motor that is converted to hydraulic power. Poor flow conditions, such as flow separation, in fluid passages contribute to hydraulic losses. Shear stress and fluid friction remove useful energy from the flow and increases the internal energy (temperature) of the system. In turbulent flow, eddies circulate flow and exchange momentum as they mix and break down. Turbulent eddies introduce additional shear stresses and contribute to internal friction losses.

3.2.1 Conservation of Mass

Mass flow through a pump is conserved. The quantity of mass entering and exiting a pump is equal. Consider a control volume around a pump impeller shown in Figure 15.

The control volume is fixed in space and cuts through the main shaft. The conservation form of the continuity equation applies to this control volume and is given in

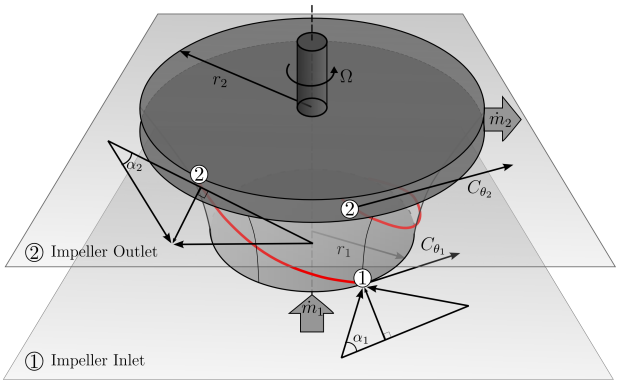

Figure 15. Control volume around pump impeller. Mass flow and angular momentum is conserved. Velocity triangles at inlet and outlet are shown.

Equation 1,

$$\frac{\partial}{\partial t}\oint_V \rho dV + \oint_A \rho \vec{C} \cdot \hat{n} dA = 0 \tag{1}$$

where $\hat{n}$ is the unit normal from the surface. The first term represents the time rate of change of mass within the control volume. Net mass in the control volume summed through a volume integral. Mass in the control volume does not change with time if the working fluid has a constant density, as is the case for hydraulic pump-turbines. Therefore, the first term in Equation 1 can be neglected for incompressible flow. The second term represents mass flow out of the control volume through the surfaces. The surface integral is zero for flow through solid surfaces along the crown and band. Therefore, only the inlet and outlet of the impeller need to be considered. For example, consider a simple case under steady conditions where flow is axial at the inlet surface and radial at the outlet surface shown in Figure 15. Here the surface integrals in Equation 1 at the pump inlet and outlet are equal and reduce to the product of density, surface area, and fluid velocity through the surface.

$$\dot{m} = \rho_1 A_1 C_1 = \rho_2 A_2 C_2 \tag{2}$$

3.2.2 Conservation of Energy

The total energy in a system is also conserved. Applying energy conservation to a one-dimensional analysis of streamlines helps illustrate how pumps transfer mechanical energy from the impeller to hydraulic energy of the fluid. The following assumptions are used to simplify analysis: 1) inviscid flow, 2) constant density fluid, and 3) steady state flow.

Bernoulli Equation Energy conservation along a streamline through a pump impeller provides a useful method of determining useful energy added to the system. An approximation of net head rise through a pump can be calculated along a streamline by applying the Bernoulli principle for inviscid flow of a constant density fluid. The resulting equation is an expression of head rise between the outlet and inlet of the pump and is shown in Equation 3. In this formulation, static pressure and dynamic pressure are reported in terms of head rise.

$$H = \frac{p_{s2} - p_{s1}}{\rho g} + \frac{C_2^2 - C_1^2}{2g} + (Z_2 - Z_1) + \frac{\Delta p_{loss}}{\rho g} \tag{3}$$

Hydraulic energy in a pumping system appears as potential energy of elevation differences (head), as kinetic energy in moving fluid (velocity head), and as potential energy in static pressure (pressure head). Net static head is the difference in elevation between the upper reservoir and tail race water surfaces, as shown in Figure 16.

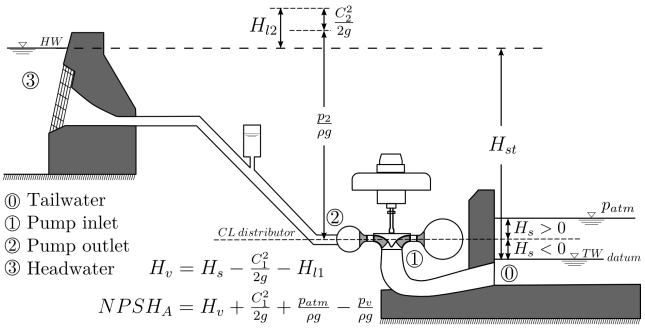

Figure 16. Representative layout of a vertical hydro pump-turbine. Common reference locations and head measurements are labeled.

In Figure 16, location ① is between the draft tube and pump inlet. Location ② is between the spiral case and penstock. The performance of pump-turbine runners is based on difference in total head rise between pump inlet and outlet at these locations. Head losses H_{l1} and H_{l2} account for friction losses in flow from locations ⓪ to ① and from ② to ③, respectively.

Curved Streamline Work done by a centrifugal pump impeller increases both kinetic and potential energy of the fluid. The impeller increase the pressure of the working fluid as it passes through an impeller by accelerating ($r\omega$) the flow along a curved path. In two-dimensional blade design theory, a curve similar to a logarithmic spiral is often used. Relative streamlines follow the blade contour in an ideal steady flow without losses and neglecting forces due to gravity. Circumferential velocity within an impeller is a function of radial location and increases from the eye to outlet of the impeller. A static pressure gradient develops perpendicular to the curved flow and increases with the square of velocity.

Consider a small fluid element moving along a streamline through a blade passage. The impeller blades force

the flow along a curved path as it moves outward radially. Even though the flow is accelerated ($r\omega^2$) as it moves radially outward, a static pressure gradient develops perpendicular to the streamline. This relationship between kinematic energy (velocity) and potential energy (pressure) along a curved streamline can be derived from balancing forces on a fluid element at a radius of curvature (r) moving at speed $C_{streamline}$ along the streamline and is presented in Equation 4.

$$\frac{dp}{dr} = \rho \frac{C_{streamline}^2}{r} \tag{4}$$

The pressure gradient along the radius of curvature, (dp/dr), in Equation 4 increases as flow accelerates along curved streamlines. The pressure gradient goes to zero as the radius of curvature approaches infinity. In other words, no perpendicular pressure gradients exist along straight streamlines in steady flow. This is a fundamental principle of how centrifugal pumps use input torque to accelerate the flow and increase the static pressure of a fluid.

3.2.3 Conservation of Momentum, Euler Equations

Flow through a centrifugal pump is complex and three-dimensional. If available head, discharge, and rotational speed are known, the performance of pumps can be approximated with a one-dimensional analysis of velocities at the leading and trailing edges of the impeller blades. Torque applied to the rotor changes the moment of momentum of the fluid as it passes through the runner. A basic one-dimensional analysis can be useful, but several conditions must be met for the analysis to be valid. Assumptions include:

1. constant density fluid (incompressible flow)
2. steady state flow
3. the system is isolated
4. the effects of gravity are negligible
5. not recirculation of flow

Apply the conservation of angular momentum to a closed control volume around an impeller, as shown in Figure /refCh3-figure:conservationAngularMomentum. The vector sum of components in a cylindrical coordinate system

Geometric consideration of velocity triangles shows

$$C^2 = W^2 + 2r\Omega C_\theta - r^2\Omega^2 \tag{5}$$

At the inlet, there are both elevation and static and dynamic pressure contributions to the head.

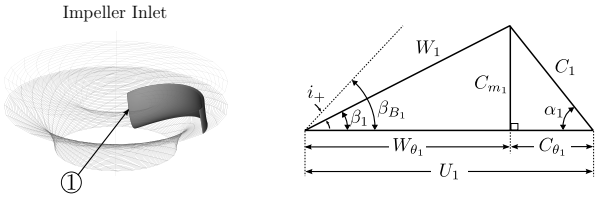

Figure 17. Inlet Velocity Triangle.

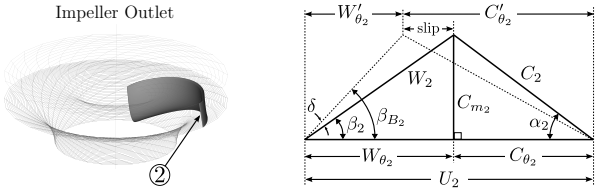

Figure 18. Outlet Velocity Triangle.

The theoretical meridional velocity is calculated by dividing the total flowrate by the area formed by rotating the leading impeller edge a complete revolution. The actual meridional velocity is higher than the theoretical value because of flow blockage due to blade thickness. The meridional velocity speeds up in the throat area as the cross sectional area of the blade passes decreases.

The absolute flow angle α_1 is approximately 90° if the inlet flow is axial. The absolute velocity C can be broken down into relative and circumferential components. The circumferential velocity is the sum of a constant circumferential velocity determined by the unit speed and radius and a component due to swirling flow. Swirling flow in the same direction as the impeller rotation causes the absolute flow angle to decrease and the relative flow shifts. Shockless entry occurs when the angle of the relative flow W matches the blade angle. The meridional velocity is determined by the flow rate and decreases as the pumped head increases. This decrease in meridional velocity increases the impingement angle. Flow can separate on the suction side of the impeller if the incident angle becomes large. Severe separation can cause flow blockage and areas of low pressure where cavitation develops. Adding additional pre-whirl C_{u1} corrects the flow angle.

Absolute tangential inlet velocity:

$$C_{u_1} = \frac{C_{m_1}}{\tan(\alpha_1)} \tag{6}$$

Absolute inlet velocity:

$$C_1 = \left({C_{m_1}}^2 + {C_{u_1}}^2\right)^{1/2} \tag{7}$$

Relative inlet flow angle:

$$\beta_1 = \arctan\left(\frac{{C_{m_1}}^2}{C_{u_1} - U_1}\right) \tag{8}$$

Incidence inlet angle:

$$i_1 = \beta_{B_1} - \beta_1 \tag{9}$$

Relative tangential inlet velocity:

$$W_{u_1} = C_{m_1} \tan(90 - \beta_1) \tag{10}$$

Relative inlet velocity:

$$W_1 = \left({C_{m_1}}^2 + {W_{u_1}}^2\right)^{1/2} \tag{11}$$

Required pump power is calculated by multiplying the Euler turbine equation by the rotation speed ω:

$$T = \rho Q(r_2 C_{\theta_2} - r_1 C_{\theta_1}) \tag{12}$$

$$Power = T\Omega = \rho Q(U_2 C_{\theta_2} - U_1 C_{\theta_1}) \tag{13}$$

$$H = \frac{P}{\dot{m}g} = \frac{1}{g}(U_2 C_{\theta_2} - U_1 C_{\theta_1}) \tag{14}$$

The useful energy transmitted to the fluid is often represented in terms of energy heads and dimensionless parameters:

$$H = \frac{C_2^2 - C_1^2}{2g} + \frac{U_2^2 - U_1^2}{2g} + \frac{W_1^2 - W_2^2}{2g} \tag{15}$$

3.3 Losses in Pump

There are many factors that affect pump efficiency. Several of the most common types of power losses in a pump are shown in Figure 19. The rotor-stator interaction and the design of the spiral case have a large impact on pressure recovery. Recirculation losses occur in the impeller at regions of stalled flow. Efficiency can be improved by reducing hydraulic losses and minimizing partload recirculation.

After passing through the impeller, accelerated fluid enters a spiral case where it decelerates. Excess kinetic energy is recovered by slowing the fluid and converting the energy to static pressure. Flow follows a curved path with a tangential velocity component (swirl) as it exits the impeller. Guide vanes in the spiral case help straighten the flow and thereby help reduce radial pressure gradients. The radial pressure decreases as the radius of curvature becomes very large ($r \to \infty$, in Equation 4.

Hydraulic losses include viscous losses due to shearing of non-uniform flows and poor incidence angles on impeller blades and guide vanes. The region between the trailing edge of the impeller and the leading edge of the guide vanes in the spiral case allows the uneven velocity and pressure distributions coming off the trailing edge to become more uniform before reaching the guide vanes.

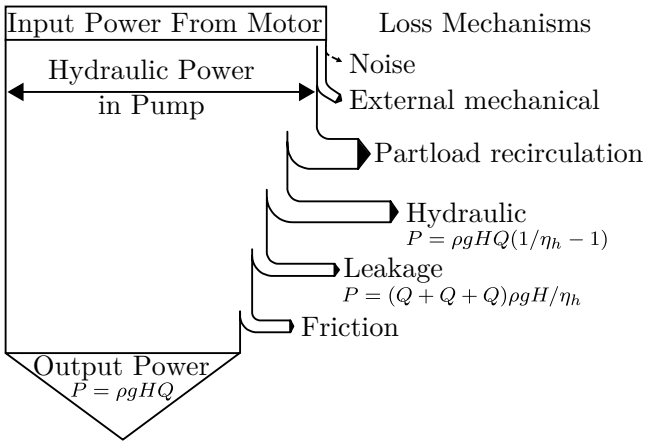

Figure 19. Common mechanical and hydraulic losses in pump impellers. Adapted from source: [37].

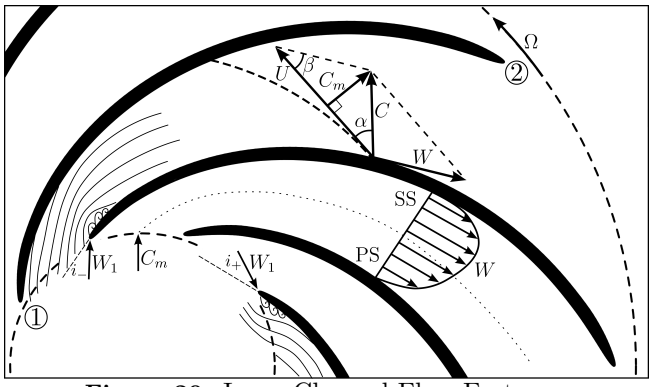

Figure 20. Inner Channel Flow Features.

Partload Recirculation Part load recirculation can occur at the inlet and outlet of the pump impeller. Recirculation is difficult to predict, but it often appears at discharge below 60 % of the design flow rate. Both flow separation and a pressure gradient perpendicular to the flow direction must be present in recirculation. Reverse flow appears near the outer walls as flow rate decreases. Energy transfered from the impeller to the flow induces pre-whirl near the outer wall. Flow enters the draft tube diffuser cone along the band and generates a positive pre-whirl that diffuses from the wall to the axis of rotation. The recirculation-induced pre-whirl helps self-correct the incident angle, and its effects reach as far as ten diameters upstream ($\frac{L}{D} > 10$) [37]. This naturally induced positive pre-whirl improves the incidence angle at low flow but causes instability and non-uniform flow. Relative velocity on the pressure side decreases as the incident angle decreases as a result of added pre-whirl from the recirculation flow. The relative velocity vector shifts toward the suction side. Pre-whirl control can be used to address part load recirculation and other hydraulic losses.

3.4 Dimensionless Parameters

Relationships between impeller speed, head, discharge, and input power can be written as dimensionless parameters. The nondimensional analysis leads to useful parameters.

Reference diameter D_{ref}:

$$D_{ref} = D_2 \tag{16}$$

Reference blade speed U_{ref}:

$$U_{ref} = \frac{1}{2}\Omega D_2 \tag{17}$$

Dimensionless flow coefficient ϕ:

$$\Phi = \frac{Q}{U_{ref} D_{ref}^2 (\pi/4)} \tag{18}$$

Dimensionless head coefficient ψ:

$$\psi = \frac{H}{U_{ref}^2/(2g)} \tag{19}$$

Dimensionless pressure coefficient c_p:

$$c_p = \frac{p - p_{ref}}{0.5\rho U_{ref}^2} \tag{20}$$

The nondimensional absolute velocity is

$$c^* = \frac{C}{\sqrt{2gH}} \tag{21}$$

The nondimensional pump specific speed is

$$\nu_s = \frac{\Phi^{0.5}}{\Psi^{0.75}} = \frac{\Omega Q^{0.5}}{\pi^{0.5}\,(2gH)^{0.75}} \tag{22}$$

Efficiency The hydraulic efficiency of a pump can be expressed in terms of the flow, head, and pressure coefficients.

$$\eta = \frac{c_p}{\psi\Phi} \tag{23}$$

Pump efficiency is defined as the ratio of the hydraulic power produced and the mechanical power that is applied to the system.

$$\eta = \frac{P_{out}}{P_{in}} = \frac{\rho g H Q}{\Omega T_{shaft}} \tag{24}$$

4. Grid Generation

The purpose of the numerical simulation is to determine performance of a pump. The pump used in this case study is from the pumping station the Grand Coulee project on the Columbia River. A pumping plant that is detached from the main generating plants houses a combination of 12 pumps and pump-turbines, shown in Figure 21. The combined pumping capacity of all units is approximately 614 MW, and the six pump-turbines can generate a combined 314 MW. The unit used for all computational simulations in this study is operated primarily as a pump. The pump draws water from a lower reservoir (Lake Roosevelt) and deliver it through a penstock to an upper reservoir (Banks Lake). Water in the upper reservoir is used for irrigation of approximately 670 000 acres of land, or can be run through other pump-turbine units in the plant to generate electricity [38]. The water levels of the upper and lower reservoirs vary seasonally and are regulated to meet generation, irrigation, recreation resource, and environmental requirements.

The computational domain consists of an elbow draft tube, pump impeller, and spiral case. The draft tube is included to allow turbulent flow to develop along the length and account for the effects of the turn of flow directly before the eye of the pump. A model of the draft tube, pump, and spiral case is built using CAD software and exported to Pointwise v16.0 meshing software. Poor tolerances from the CAD software are resolved, and water-tight surface meshes are generated. Volume meshes were built from the surface meshes. Individual components are modeled with boundary-fitted, three-dimensional structured grids of hexahedral cells. The resulting volume meshes use in the spiral case, impeller passage, draft tube, and draft tube cone are shown in Figures 28, 29, 32, and 31, respectively. Surface meshes on the impeller blades and spiral case are shown in Figure 30 and Figure 33.

4.1 Coordinate System

The pump axis of rotation is aligned along the z-axis in a Cartesian coordinate system shown in Figure 22. The centerline of the draft tube lies in the xz-plane. The centerline of the exit diffuser and piping lies in the xy-plane. Several locations of interest in the draft tube and spiral case are labeled in Figure 22. Pressure rise across the pump is defined by measurements at section DD and section AA. The draft tube cone begins at section BB. A conical exit diffuser extends from the spiral case at section AA to the beginning of circular piping at section CC.

A meridional projection of the pump is shown in Figure 23. Common reference diameters are labeled. The diameter of the trailing edge of the impeller blade at the centerline of the pump, D_2, is used in dimensionless parameters. The axial position of added blowing jets is also shown. Eight jets are equally spaced circumferentially around the draft tube cone and have a height of Z_{jet}.

4.2 Cell Types

The computational domain must be spatially discretized in order to calculate a numerical solution. Common

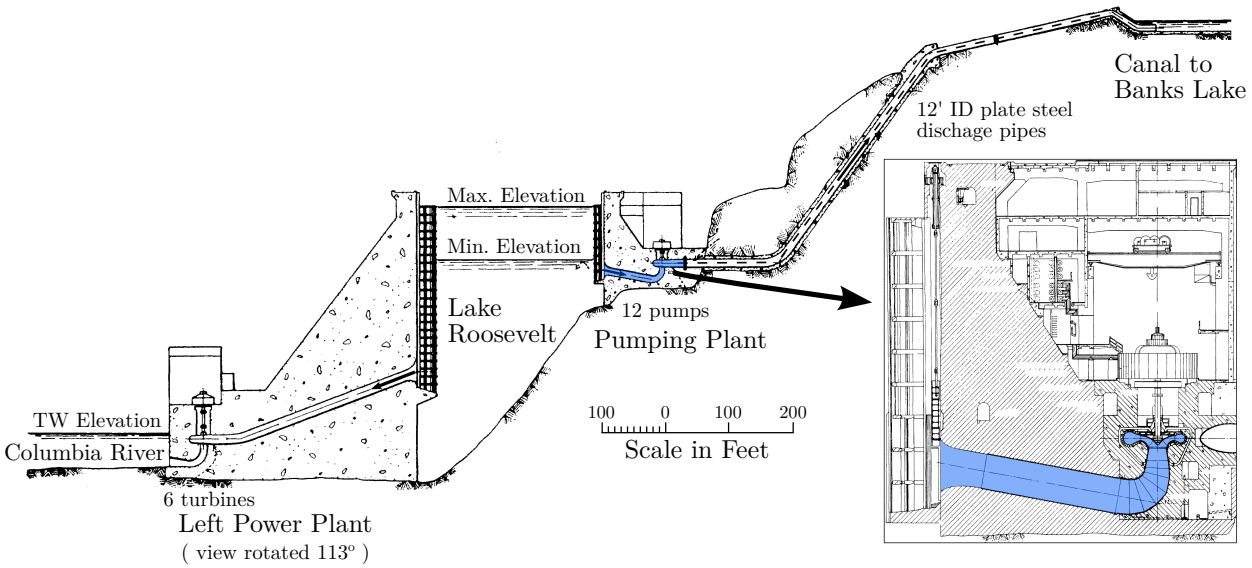

Figure 21. Computational domain that is modeled includes the draft tube diffuser, impeller, and spiral distributor of a pump from the Grand Coulee project on the Columbia River. Adapted from source: [39].

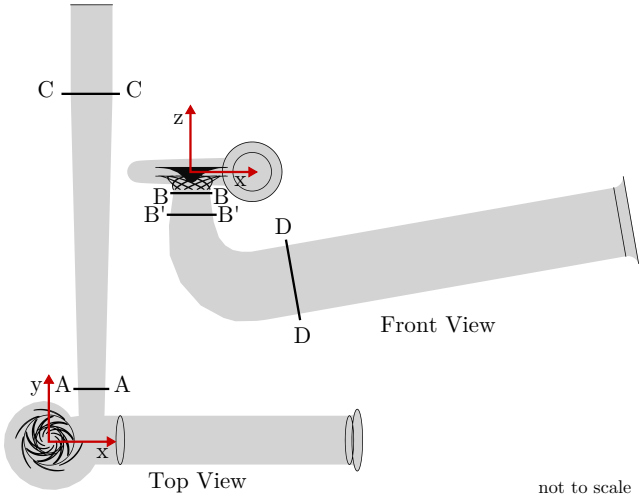

Figure 22. Coordinate system and location of reference cross sections used in analysis.

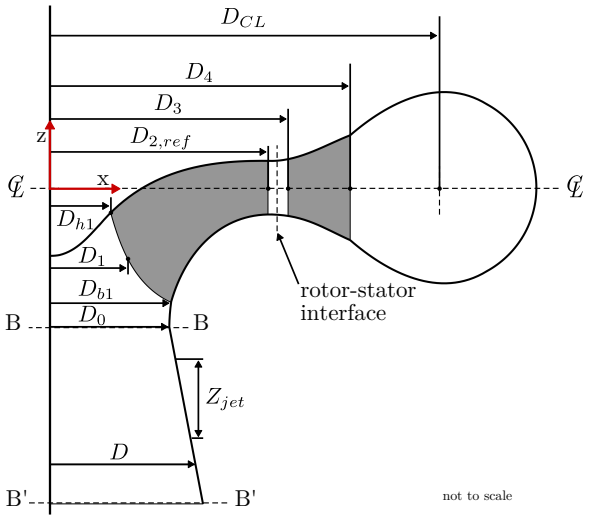

Figure 23. Reference diameters and location of added jets.

discretization methods used in CFD codes include finite difference, finite element, finite volume, and spectral methods. Finite difference methods discretize a differential form of the governing Navier-Stokes equations on nodes of a grid. Partial derivatives are often approximated by applying a truncated Taylor series expansion. Finite volume methods are similar to finite difference methods, with the main difference being the form of the Navier-Stokes equations. Finite volume methods discretize an integral form of the governing equations over a control volume (mesh cell) instead of the differential form discretized over mesh nodes. Using the integral form of the governing equations ensure that mass and momentum are always conserved in cells.

In this study, the collocated finite volume method is applied to structured hexahedral grids. Representative finite volume cells are illustrated in Figure 24. Each hexahedral control volume element is built from six faces and eight corner nodes. The conservation equations are integrated over the surfaces surrounding the center of the control volume. Values of flow variables such as the magnitude of velocity components, pressure, and turbulent parameters are stored at cell centers (P). Some variables, such as velocity, depend on the flux through the cell surfaces. Quadrature using various stencils of neighboring nodes are used to approximate the integrals at control surfaces.

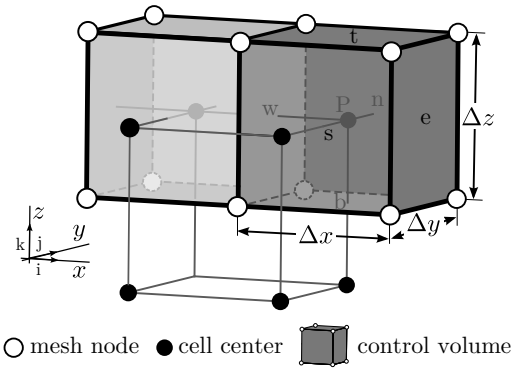

Figure 24. Control volumes built from hexahedral structured mesh. A two-dimensional grid in the xy-plane would consist of the **n**orth, **s**outh, **e**ast, and **w**est faces. A three-dimensional grid adds a **t**op and **b**ottom face to create a volume.

4.3 Grid Topology

A multiblock meshing strategy is used. The spiral case, impeller, and draft tube are separate zones. Each zone is built from smaller cell blocks. For example, the full impeller is modeled by duplicating the grid of a single, periodic blade passage. Point-to-point grid matching is used at all internal interfaces, except interfaces between moving and stationary grids. Also, a nonconformal mesh is used in the draft tube cone to accommodate inlet jets. An O-H grid is used to fit the circular draft tube and outlet diffuser with a structured grid. A structured O-grid block is constructed around impeller blades and guide vanes. Grid spacing within the O-grid boundary layer block is controlled manually by adjusting node spacing and can be modified without disturbing the main grid. A H-style grid connects the block surrounding the blades with the bounding walls. This topology allows for fine control of grid quality and spacing near walls.

4.4 Grid Spacing at Wall

Special consideration of perpendicular grid spacing near walls is needed in wall-bounded turbulent flow. It has been widely observed that flow characteristics near the wall depend on the normal space from the wall. Nondimensional parameters are used to describe and scale quantities within a turbulent boundary layer. A nondimensional distance perpendicular to a wall is given as y_+.

$$y_+ = \frac{y u_*}{\nu} \tag{25}$$

A nondimensional characteristic velocity is given as u_+.

$$u_+ = \frac{u}{u_*} \tag{26}$$

Both of these parameters are scaled by the shear stress at the wall. This scaling is done through the shear velocity, u_*. This friction velocity scales the magnitude of velocity fluctuations in turbulent flow and is defined as

$$u_* \equiv \sqrt{\frac{\tau_w}{\rho}} \tag{27}$$

where $\tau_w = \mu \partial u / \partial y|_0$ is the viscous shear stress at a wall. This friction velocity has the units of velocity and is a measure of velocity variation due to turbulence.

This is known as the law of the wall, as shown in Figure 25. Flow in a small layer closest to a wall is most affected by viscous forces and is consistent with laminar flow. Turbulence becomes more important away from the wall. Turbulence begins to affect the flow away from the wall. Flow is fully turbulent in the core flow. This is the outer layer.

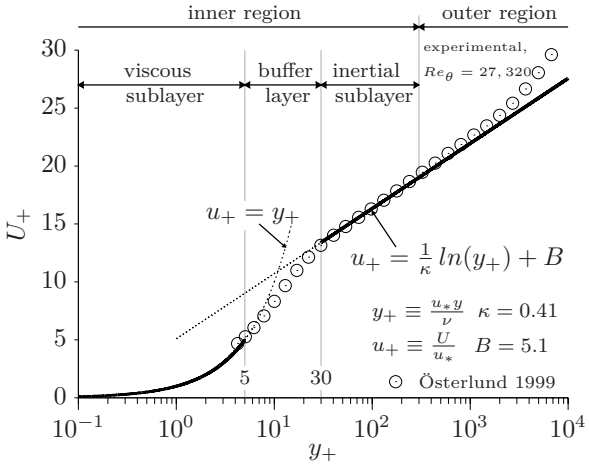

Figure 25. The law of the wall and regions of a turbulent boundary layer. Experimental velocities at $Re_\theta = 27,320$ are from [40].

A boundary condition appropriate for low Reynolds number flow is applied if the mesh is fine enough ($y_+ < 5$) near the wall. Otherwise, the first cell center should be $30 < y_+ < 300$ and wall functions are applied.

Attempts are made to keep the cell centroid of the first layer of cells is within the viscous sublayer of the boundary layer ($y_+ < 30$) at all walls. The fine near-wall spacing is evident on the band around the blades in Figure 27a.

4.5 Grid Quality

The quality of the computational grid has a direct impact on the accuracy of the numerical solutions. Poor quality cells can hinder solver convergence and lead to interpolation errors between cell center and faces. Poor quality cells include those that are highly skewed, warped, non-orthogonal, and stretched.

The histogram in Figure 26 shows the relative quantity of cells in the draft tube, draft tube cone, runner, and spiral case that exhibit various levels of skewness. The number of cells in each histogram bin are shown as a percent of the total cells in each zone. Equilateral skewness is a ratio of cell angle and the angle of an equivalent equilateral cell. Equilateral skewness can vary from 0 (an equilateral element) to 1. It is desirable to have low skewness values close to zero. Equilateral skewness is below 0.7 everywhere except a few cells in the crotch region of the spiral case. This is an acceptable level of skewness.

Centroid skewness is a measure of cell orthogonality and measures the collinearity of a surface normal vector ($\hat{n}$) and a vector ($\vec{v}$) that connects the cell centroid and face centroid. These two lines are collinear ($\hat{n} \cdot \vec{v} = 1$) in non-skewed cells, and perpendicular ($\hat{n} \cdot \vec{v} = 0$) in collapsed cells. Centroid skewness of a cell is defined as the difference between the dot product ($\hat{n} \cdot \vec{v}$) of an ideal non-skewed cell and the maximum dot product of the cell. Using this definition, centroid skewness values also range from 0 to 1. All cells in the computation domain have a centroid skewness below 6. Levels of centroid skewness for various grid zones can be found in Figure 26.

Greater orthogonaliy in boundary layer meshes is achieved using hexahedral cells rather than tetrahedral cells. However, some cells in the boundary layer mesh exhibit high aspect ratios in the direction of flow. Higher than desirable aspect ratios are tolerated in the boundary layer region to limit the total number of cells in the simulation.

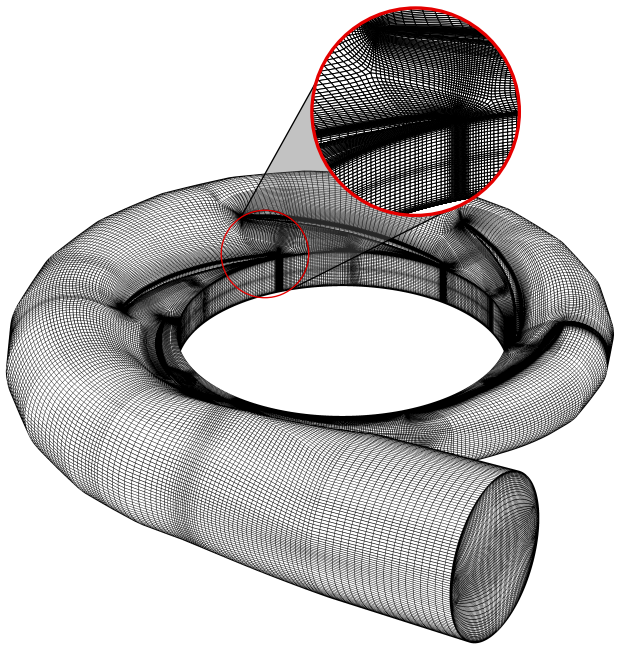

Figure 28. Structured volume mesh in spiral case. Mesh details at the leading and trailing edges of a guide vane are highlighted.

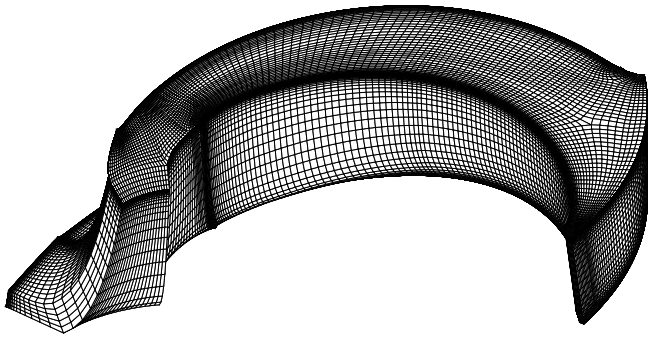

Figure 29. Structured volume mesh through single impeller blade passage. Blade surfaces are split and the leading and trailing edges. The volume mesh shown here is duplicated 9 time around the cell zone in Figure 31 to form a complete full-wheel impeller.

5. CFD Solver Setup

5.1 Solver

ANSYS® Fluent is a commercial finite volume CFD code. A cell-centered, co-located finite volume scheme provides the basis for generating system of linear equations. Fluent offers a density based solver, and a pressure based solver. A density based solver is typically used for compressible flows at high speeds (large Mach number). All simulations in the current study are pressure-based solutions. Several algorithms are available for solving the system of equations, but the general solution process in Figure 34 is followed for the pressure-based solver. Velocity components can be solved from the flux through control volume surfaces. The continuity equation is solved for a pressure corrections factor. Velocity, pressure, and mass flux are updated before solving turbulence equations. This general procedure is repeated until convergence is achieved.

Fluent uses a cell centered finite volume approach to solving the governing equations and stores all variables at cell centers, a co-located scheme. This requires interpolation of flux-based velocities at cell faces at cell centers. Fluent solves the system of algebraic equations iteratively.

5.2 Rotor-Stator Interfaces

5.2.1 Frozen Rotor Simulations

Frozen rotor simulations approximate unsteady problems as steady-state problems relative to a local rotating reference frame. This approximation is achieved by fixing the rotor and adding Coriolis and centripetal acceleration forces to the governing equations. The problem is then solved individually with respect to appropriate reference

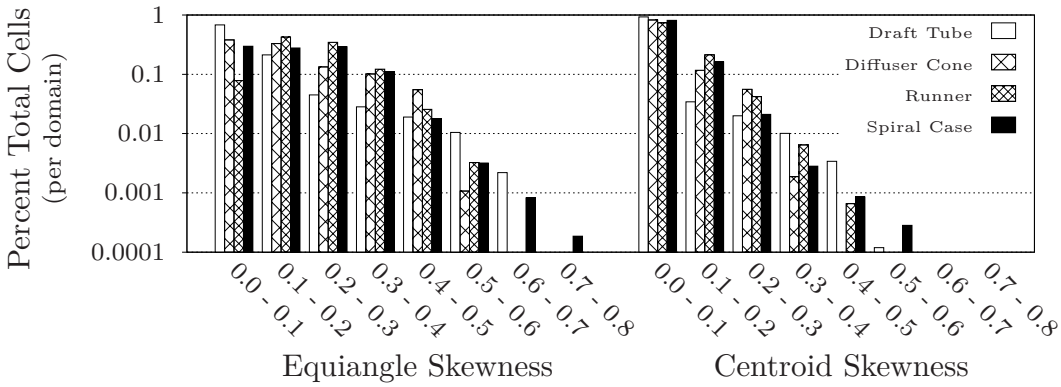

Figure 26. Equiangle and centroid cell skew for individual computational domains of structured cells.

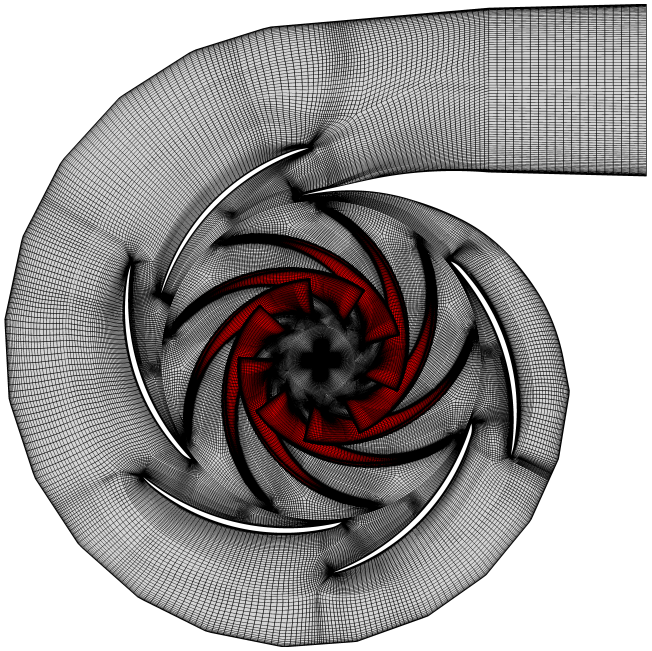

Figure 30. Structured mesh on impeller blade surfaces and spiral case. The spiral case mesh shown here is located on a plane perpendicular to the axis of rotation at the spiral case centerline.

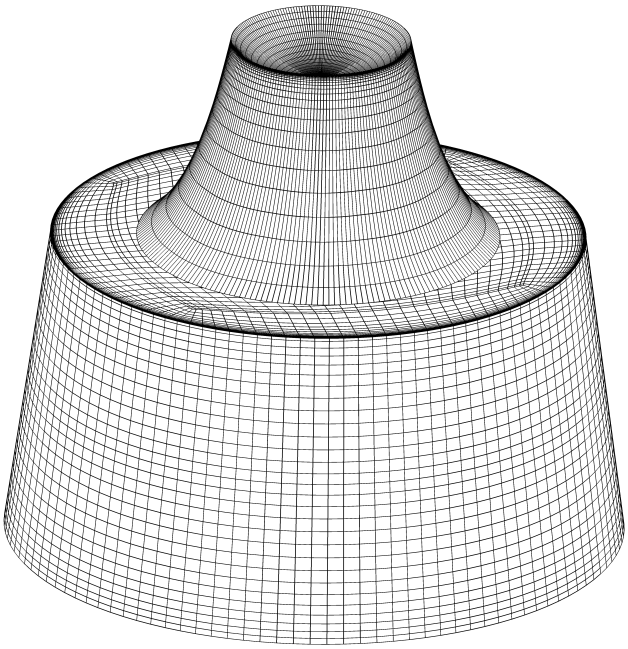

Figure 31. Structured volume mesh on draft tube cone. The concave depression located at the top of the cell zone is the nose cone surface of the impeller crown.

frames. The solution of a frozen rotor simulation is highly dependent on the position of the rotor. Flow features that depend on the bulk flow, such as vortex shedding, can be captured with this solution method.

The frozen rotor simulation is applied in Fluent as a multiple reference frame model. Scalar properties, e.g., pressure, density, temperature, turbulent kinetic energy, are passed directly from one cell to another across the interfaces between reference frames. Relative vector properties (velocity and velocity gradients) must be adjusted at the interface because of the rotating reference frame. Fluent maintains continuity of absolute velocity across MRF interfaces. These approximations are appropriate for turbomachines where rotor-stator interactions are uncomplicated. MRF solutions can be used as the initial conditions for a sliding mesh model. Unsteadiness due to rotor-stator interactions cannot be modeled.

5.2.2 Mixing Plane Simulations

The mixing plane circumferentially averages flow quantities at the interfaces.

A mixing plane model (MPM) averages the outlet of one zone to use as the inlet to an adjacent zone. The mesh is physically stationary. Each zone can have a different grid spacing at the interface. This averaging adds computation time to the problem but results in more accurate solutions. Mixing plane modeling is a steady-state approach to solving an unsteady problem. This model can still model unsteady phenomenon like vortex

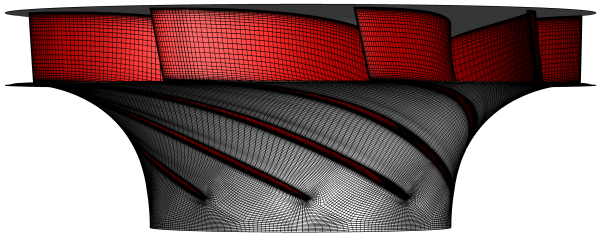

(a) Structured surface mesh on band.

(b) Grand Coulee Pump No. 1

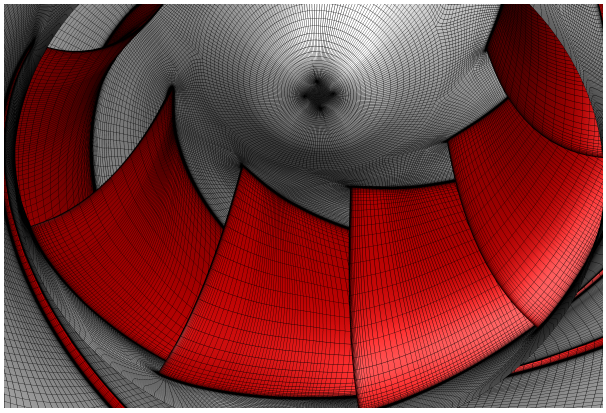

(c) Structured mesh on crown and blades.

(d) Nose cone and suction side of blade.

Figure 27. Structured mesh and pump photographs. Photo source: [41].

shedding that depends entirely on the flow. However, any unsteadiness as a result of stator/rotor interaction cannot be captured with this model. Fluent uses circumferential averaging across MPM interfaces.

5.2.3 Sliding-Mesh Simulations

Sliding-mesh simulations offer a fully unsteady solution and is the most accurate method for calculating unsteady flow. The rotor mesh advances each time. A solution is converged to a specified level each time step. Quantities are time-averaged over at least one revolution after a steady-state is reached.

A sliding mesh model (SMM) physically rotates the mesh in time and is capable of capturing unsteady interactions between the stator and rotor zones. An interface must be defined between a stationary and rotating mesh. This model is required to model unsteadiness as a result of rotor-stator interaction. Cell nodes are updated as a function of time.

5.3 Computing Resources

Calculations are run on remote servers managed by the Research Computing and Cyberinfrastructure unit at The Pennsylvania State University. Compute nodes are Intel Xeon X5675 six-core 3.06 GHz processors running in parallel. Parallel communication is through 40 Gb/s InfiniBand connections.

6. Simulation Results

6.1 Grid Independence Study

A grid dependency study is completed to quantify discretization error. Richardson extrapolation is a method used to determine discretization error associated with changing grid resolution and extrapolating the results to a theoretical grid with infinitesimal control volumes. Roache's Grid Convergence Index (GCI) is calculated and used to establish approximate ranges of numerical uncertainty. The goal of these methods is to estimate the numerical error over entire computational domain and confirm the expected order of convergence.

6.1.1 Discretization Error

The solution of a numerical simulation can vary depending on the discretization technique and grid resolution. Discretization errors arise from converting the continuous derivatives and integrals of the partial differential governing equations into discrete algebraic equations.

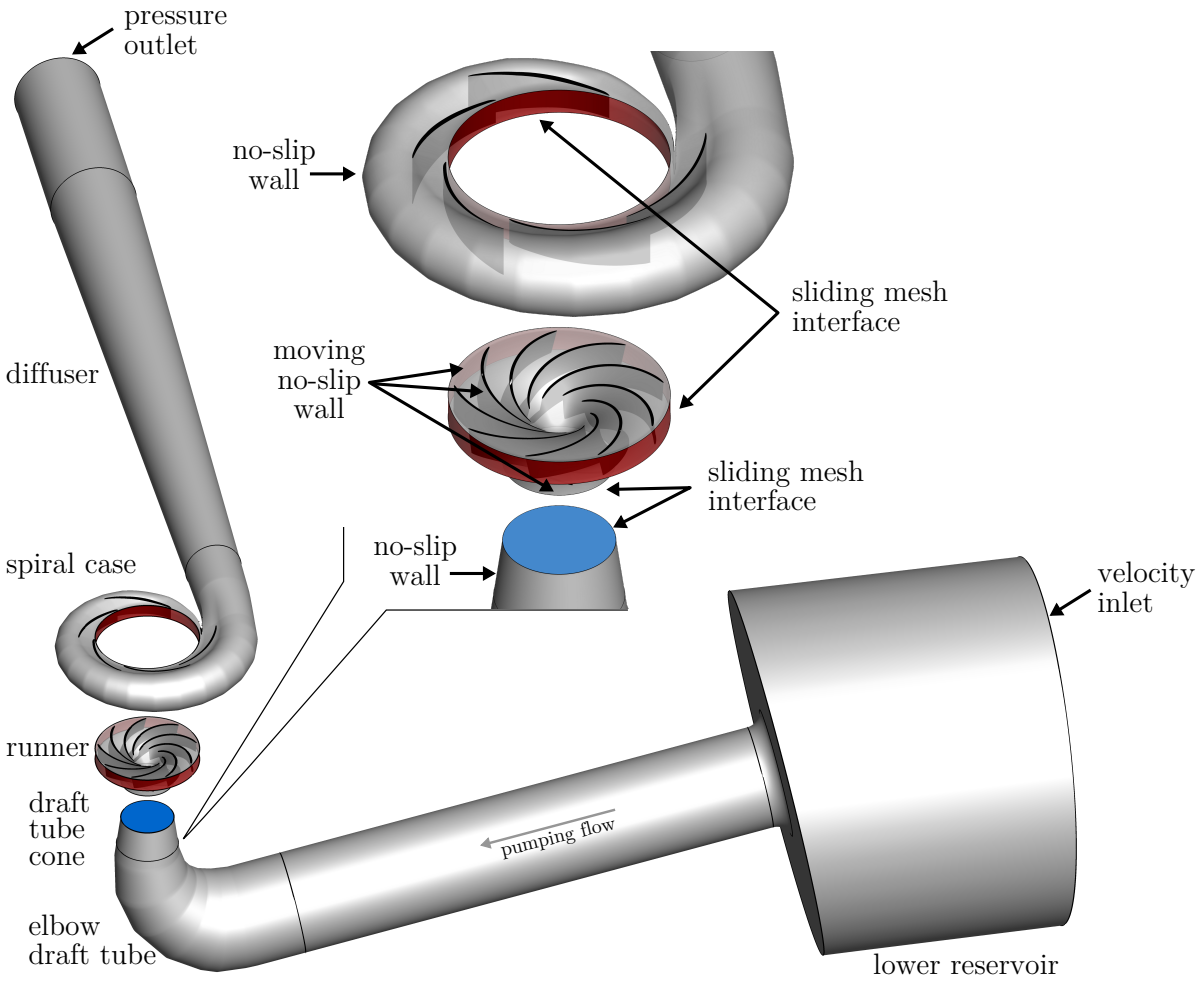

Figure 35. Boundary Conditions.

Discretization error arises from solving these discrete equations at a grid of individual points. In general, closely spaced grids produce more accurate solution than coarse grids. It is important to use an appropriately sized grid to resolve flow features while maintaining reasonable computational time.

Discretization error ε_h^d on a mesh with grid spacing h is defined as the difference between the solution (ϕ_h) of the discretized equations and the solution ($\tilde{\phi}$) of the exact mathematical equations, where ϕ represents a scalar variable of interest. This definition of discretization error is defined in Equation 28.

$$\varepsilon_h^d = \tilde{\phi} - \phi_h \tag{28}$$

6.1.2 Richardson Extrapolation

Richardson extrapolation is applied to three grids with progressively fine spatial resolution. Rounding error and computational cost limits the minimum practical size of grid spacing. The grid resolution cannot practically be halved in each test due to limited computational power.

Richardson extrapolation can be used to approximate the solution in the limit as grid spacing approaches zero. The solution on an infinitely fine grid is estimated by extrapolating from a series of solutions computed on grids with greater spacing. In the current investigation, three grids with progressively fine spacial resolution resolutions are used to establish the order of convergence and to estimate the numerical error. Cell counts for individual zones of each grid are displayed in Table 2.

Richardson extrapolation is a well-known technique used to evaluate error in the solution to discretized differential equations and to achieve higher order solutions than the original equations [43, 44]. It works on any discretization scheme (finite difference, finite volume, finite element) because it uses power series expansion of solutions on several grids with different refinement levels, independent of the choice of discretization scheme.

Richardson extrapolation requires that a number of conditions are met. First, the underlying function must be smooth and continuous. This condition ensures that derivatives exist in expanded Taylor series. The method

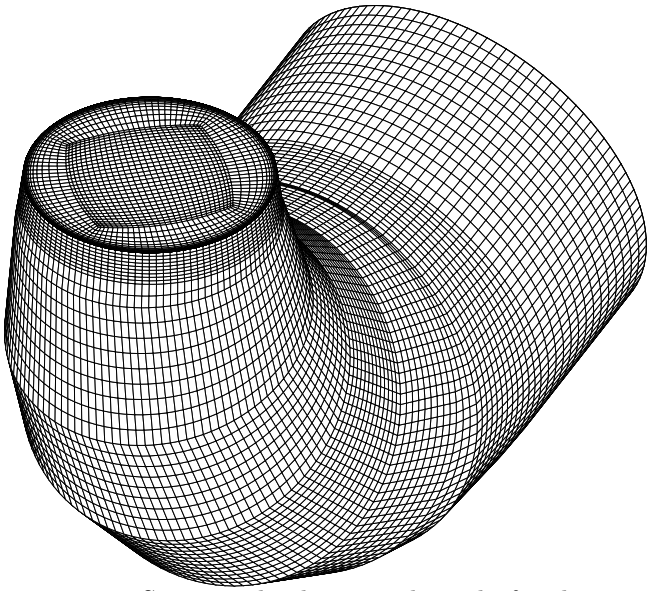

Figure 32. Structured volume mesh on draft tube elbow.

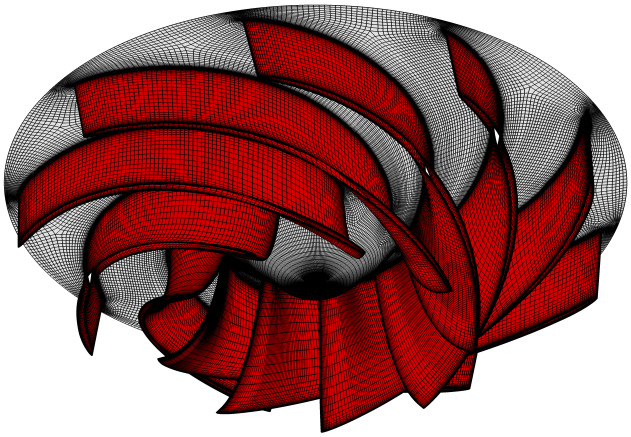

Figure 33. Structured surface mesh on impeller crown and blades.

breaks down if singularities or discontinuities are present. Second, the extrapolation is valid only in regions where the discretization error behaves asymptoticly. That is, the lower-order error terms of the discretization error power series dominate and consequently, higher-order terms may be neglected with minimal impact on the result. Finally, the convergence rate of the discretization scheme must be known on at least three similar refined grids with regular spacing refinement ratios. The observed order of accuracy should match the expected accuracy of the discretized equations. The Guidelines outlined by Obkerkampf and Roy [45] and by Freitas et al. [46, 47] are used to estimate discretization error. A brief summary of the procedure is provided below.

Consider the discretization error of three progressively refined grids with node spacing h, where $h_1 < h_2 < h_3$.

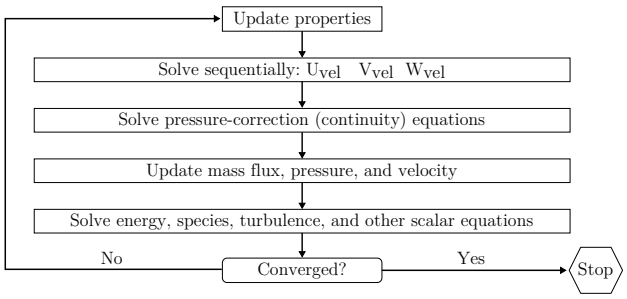

Figure 34. Pressure based solution procedure used in ANSYS® Fluent, Release 14.0 solver. Source: [42]

Table 2. Mesh refinement used in Richardson Extrapolation grid convergence analysis.

	Grid Refinement Levels		
Domain	Grid 1	Grid 2	Grid 3
Tailrace	160,254	182,400	450,302
Draft Tube	685,125	868,352	2,078,209
Draft Tube Diffuser	176,128	368,640	861,930
Nose Cone	263,802	1,081,377	2,195,523
Blade Passage (x9)	4,417,920	18,211,158	36,730,998
Spiral Case	3,403,642	2,004,728	2,004,728
Diffuser	809,028	510,176	510,176
Total	9,915,899	23,226,831	44,831,866

The grid refinement factor, r, is defined as the ratio of a coarse grid spacing and fine grid spacing.

$$r = \frac{h_{coarse}}{h_{fine}} \tag{29}$$

If the grid refinement factor is constant between the coarse and medium and the medium and fine grids, the level of grid resolution can be expressed as multiples of the most fine grid. However, in this case, the grid refinement ratios are not equal, and $h_3 = r_{32}h_2$, and $h_2 = r_{21}h_1$. The solution of the fine grid (ϕ_1) and the medium grid (ϕ_2) can be written as a power series expansion around the exact solution for scalar variable $\tilde{\phi}$.

$$\phi_1 = \tilde{\phi} + g_p (h_1)^p + g_{p+1} (h_1)^{p+1} + O\left[(h_1)^{p+2}\right] \tag{30}$$

$$\phi_2 = \tilde{\phi} + g_p (h_2)^p + g_{p+1} (h_2)^{p+1} + O\left[(h_2)^{p+2}\right] \tag{31}$$

Here, the g variables are constants independent of grid size and could be the derivatives of a Taylor series expansion. The power of the leading-order truncation error term, p, is the observed rate of convergence and is easily calculated if a third grid is used in the analysis. The node spacing of the coarser grid is related to the fine grid by $h_2 = r_{21}h_1$. The constant, g_p, can be

eliminated by neglecting higher order terms and combining Equations (30) and (31). An assumption is made that the leading order truncation term dominates the discretization error. If higher order terms are neglected, eliminating g_p constants and rearranging terms produces a new expression for the exact solution to the discretized governing partial differential equations. The Richardson extrapolation of the exact solution is then,

$$\tilde{\phi}_{exact,RE} = \phi_1 + \frac{\phi_1 - \phi_2}{r^p - 1} \tag{32}$$

The approximate relative error is the error between the two grid solutions relative to the solution from the fine grid. The solution from the fine grid is presumably the more accurate solution.

$$\varepsilon_{21}^a = \left| \frac{\phi_1 - \phi_2}{\phi_1} \right| \tag{33}$$

Similarly, the extrapolated solution in Equation (32) is used with the fine grid to calculate an extrapolated relative discretization error.

$$\varepsilon_{21}^{ext} = \left| \frac{\tilde{\phi}_{RE} - \phi_1}{\tilde{\phi}_{RE}} \right| = \left| \frac{\phi_2 - \phi_1}{\tilde{\phi}_{RE}(r^p - 1)} \right| \tag{34}$$

Three-dimensional Grid A representative grid metric for one-dimensional node spacing must be defined for three-dimensional grids. The following definition uses the cubic root of the average cell volume.

$$h = \left[\frac{1}{N} \sum_{i=1}^{N} (\Delta V_i) \right]^{1/3} \tag{35}$$

In Equation 35, V_i is the volume of the ith cell. N is the total number of cells in the computational domain. This representative grid size is based on average volume and can thereby be used on structured or unstructured grids. Refinement factors in Equation (29) can now be calculated. Based on experience, Freitas et al. suggests that the grid refinement factor greater than 1.3 should be maintained between three successively refined grids ($h_1 < h_2 < h_3$).

A general extension of Richardson extrapolation can be used in cases where refinement ratios differ, e.g., $r_{21} = h_2/h_1$ is not equal to $r_{32} = h_3/h_2$. Freitas et al. [47] recommend the following method to calculate observed convergence, p, for nonuniform grid ratios:

$$p = \frac{\ln \left| \frac{\phi_3 - \phi_2}{\phi_2 - \phi_1} \right| + q(p)}{\ln (r_{21})} \tag{36}$$

where $q(p)$ is

$$q(p) = \ln \left(\frac{r_{21}^p - s}{r_{32}^p - s} \right) \tag{37}$$

and

$$s = 1 \cdot \text{sign} \left(\frac{\phi_3 - \phi_2}{\phi_2 - \phi_1} \right) \tag{38}$$

Equations (36)-(38)are solved iteratively. No iteration is needed if grid refinement ratios are equal, $r_{21} = r_{32}$, because $q(p)$ is zero.

6.1.3 Grid Convergence Index (GCI)

It is useful to report discretization error and along with some measurement that evaluates the uncertainty in grid independence study results. Roache [48] developed a Grid Convergence Index (GCI) to report discretization error in a method that accounts for the grid refinement ratio and the observed order of convergence. The GCI method relates discretization error from grid independence studies to a expected outcome of a second order method on grids with a constant refinement ratio of two. The definition of GCI used in this paper is essentially the approximated relative error from Richardson extrapolation multiplied by a correction factor.

$$GCI = \frac{Fs}{r^p - 1} \left| \frac{\phi_1 - \phi_2}{\phi_1} \right| \tag{39}$$

Here, Fs is a constant factor of safety introduced to the error band with the purpose of achieving 95 % confidence in the calculated band of uncertainty. The safety factor is based on empirical data. Roache [49, 50] recommends that a factor of safety of 3 should be used when the order of convergence is known and only two different grids are used. A safety factor of $Fs = 1.25$ is used to calculate the error band if three or more grids are used to evaluate the observed order of convergence. Based on these recommendations, $Fs = 1.25$ is used as the factor of safety. Some practitioners omit the normalizing ϕ in the denominator of Equation 39 so that the GCI values have the same units as the parameter being evaluated.

The GCI is a measure of relative uncertainty in the solution. For example, consider the fine grid GCI at section AA, $GCI_{21} = 0.0181$. A GCI of 0.0181 indicates that it is reasonable to approximate, with 95 % confidence, 1.8 % uncertainty in the measurement of pressure on the fine grid at section AA. Additional GCI values are located in Table 3.

One of the assumptions for Richardson extrapolation is that the grids should fall withing the asymptotic range of convergence. This condition can be verified by evaluating GCI between three grids to determine if they are sufficiently refined to approach the asymptotic range of

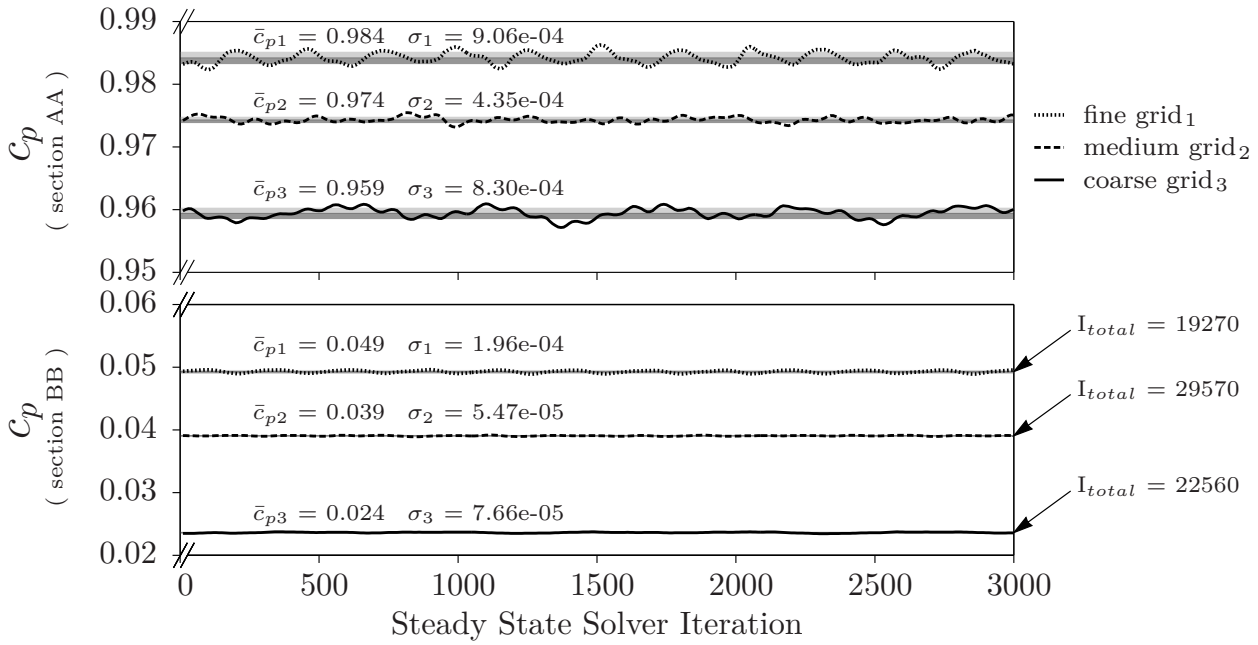

Figure 36. Integrated pressure coefficients at inlet (section BB) and outlet (section AA) of the impeller. Convergence history of last 3000 iterations of steady state solution for three grids used in grid dependency study. The average pressure coefficient and one standard deviation of the fluctuating convergence is displayed.

Table 3. Richardson extrapolation of pressure coefficient at measuring sections BB and AA.

Variable	BB	AA	Description
r_{21}	1.325	1.325	ratio (medium/fine)
r_{32}	1.293	1.293	ratio (coarse/medium)
p	1.877	1.872	observed convergence rate
ε_{21}^{da}	0.207	0.0100	approximate relative error
ε_{21}^{dext}	0.230	0.0143	extrapolated relative error
GCI_{21}	0.373	0.0181	medium to fine grid GCI
GCI_{32}	0.798	0.0310	coarse to medium grid GCI
	1.262	1.0101	$GCI_{32}/r^p GCI_{21}$

convergence. If three grids have constant grid refinement ratios, $r = r_{21} = r_{32}$, and are in the asymptotic range of convergence, then the GCI between the grids differ by a factor of r^p [49].

$$GCI_{32} = r^p GCI_{21} \left| \frac{\phi_1 - \phi_2}{\phi_1} \right| \tag{40}$$

The observe order of convergence, p, must be calculated independently from Equation 40 by using all three grids. This relationship is used to confirm that the grids are within the asymptotic range. Although refinement ratios are not equal in Table 3, we use $r = 0.5\,(r_{21} + r_{32}) = 1.31$ to evaluate Equation 40. By extension, the discretization error converges asymptoticly if $GCI_{32}/\,(r^p GCI_{21}) = 1.0$. The results of this calculation are located in Table 3. Based on the result at section AA (1.010), discretization error converges nearly asymptotically with decreasing node spacing at the exit of the spiral case. However, evaluating Equation 40 at section BB is less conclusive.

The discretization error is plotted on a log-log scale as a function of grid spacing in Figure 37. The convergence rate is visualized by plotting on a log-log scale.

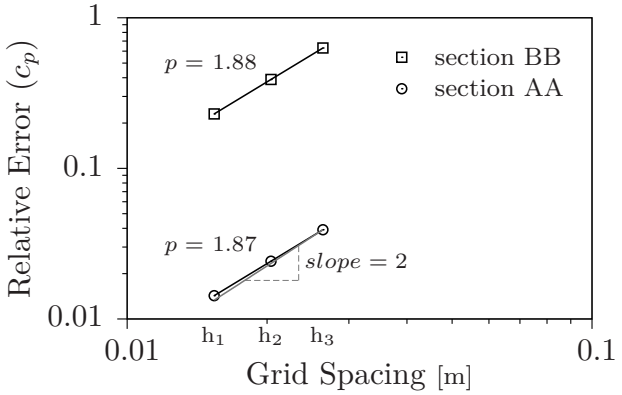

Figure 37. Relative discretization error for three successively refined grids. Mean total pressure of a steady state solution is integrated over the inlet (section BB) and the outlet (section AA) of the pump.

The slope of this plot is equivalent to the observed convergence rate, p, provided that the grid refinement is performed within the asymptotic range of convergence. The relationship between the convergence rate and the

slope of the log-log plot is made clear by taking the log of both sides of Equation (30) and neglecting higher order terms.

$$log\left(\varepsilon^d_{h_1}\right) = p \cdot log(h_1) + log(g_p) \tag{41}$$

The observed rate of pressure convergence for total pressure at two sectioned measuring planes is shown in Figure 37. The observed rate of pressure convergence is 1.88 at the interface between the draft tube and impeller (section BB). The relative discretization error is over an order of magnitude greater near the inlet of the pump.

The observed rate of pressure convergence is 1.87 at the outlet of the spiral case (section AA). The relative discretization error is lower due to greater pressure. The absolute error remains approximately the same between the two sections, but the denominator in Equation 33 is much greater at the outlet of the pump.

A fixed rotor simulation is run on the three grids listed in Table 2. The pressure coefficient at two measurement sections is plotted in Figure 36. It appears that the pressure fluctuations at the outlet of the spiral case (section AA) are larger than at the interface between the draft tube cone and the impeller (section BB). The same pressure scale is used in both plots, but the total pressure is much larger at the outlet of the pump. Mean pressure coefficients and one standard deviation for 3000 iterations are displayed on the plots. Richardson extrapolation is performed with the mean pressure coefficients.

The numerical method converges at an apparent rate of $p = 1.9$. This is the expected convergence for a second order scheme and is conformation that a second order scheme is used. The convergence rate describes how quickly the solution converges to the exact solution, not necessarily the accuracy of the solution.

The discretization error decreases quickly as the grid resolution increases (more nodes). The extrapolated pressure coefficient at section BB is $\tilde{\bar{c}}_p = 0.0640$, and the estimated relative error for the fine mesh is approximately 23 %. The relative error at section AA is 1 %. The absolute error is a full order of magnitude lower at the outlet than the inlet. The relative error is further separate because the total pressure is much greater at the outlet. This disparity in relative error may be attributed to the larger pressure at the outlet of the pump. The inlet section is also located at a cell zone interface.

While the pressure at the inlet of the pump is lower than at the outlet of the pump, the relative error is approximately twenty times larger. The absolute error remains on the same order, but the relative error is larger at the inlet. This is not unexpected, because the flow can be unsteady and experience pressure pulsations because of the proximity to the leading edge of the impeller blades.

Adding more nodes would increase the computational cost of the solution with minimal improvement in accuracy. This makes the Richardson method valuable for estimating exact solutions from sufficiently refined grids. The graph indicates that the grids are sufficiently fine and are within the range of monotonic convergence.

6.2 Flow Rate Selection

First, fixed rotor simulations are run on a single blade passage. The inlet swirl is specified by adjusting the velocity profile at the inlet of the impeller. Whirl velocity is increased linearly from zero at the axis of rotation to maximum pre-whirl at the draft tube wall.

Next, an attempt is made to design adjustable inlet guide vanes capable of matching flow angles and controlling inlet whirl at off-design points. One of the objectives of pre-whirl control is to reduce the effects of recirculation at low flow conditions to improve pump operation. Instead of using physical guide vanes to control pre-whirl and to influence angular momentum in the draft tube cone, blowing is introduced through jets located in the wall of the draft tube cone.

The computational domain is expanded to include the complete draft tube, impeller blade, and spiral case shown in Figure 35. The draft tube cone is also modified to include jets. Eight rectangular jets are equally spaced around the perimeter. This is the grid on which most of the simulations are run, and the grid independence study is applied to this grid.

Two main advantages of active control are the flexibility to adjust the swirl as the operating conditions change and the option to turn off any adjustments at BEP. Adding flow near the wall also could help prevent recirculation observed near the diffuser wall at low flow conditions. A small percent (1 % to 5 %) of the total flow is directed through the slots to influence the magnitude of pre-whirl and thus angular momentum. Global discharge is preserved at desired operating conditions. A fixed rotor simulation with multiple reference frames is used in these simulations.

Six flow rate cases are tested:

Table 4. Tested Flow Rates

Case Name	$\%Q$	Φ
Case01	0.418	0.0294
Case02	0.593	0.0417
Case03	0.709	0.0499
Case04	0.867	0.0610
Case05	1.042	0.0733
Case06	1.235	0.0869

Pre-whirl is added by changing angular momentum in the draft tube cone by blowing through slits in the wall of the draft tube cone, as shown in Figure 38. Positive swirl angles are defined as angles that add circumferential

velocity component in the same direction as the impeller rotation, and negative swirl angles are defined as those that cause reverse whirl in the opposite direction as impeller rotation. Peripheral jets are chosen to allow for active control of angular momentum and axial flow in the draft tube cone. Blowing is considered positive if pre-whirl is in the same direction as the rotor and negative if it is in the opposite direction. Negative pre-whirl adds energy to the flow in accordance with the Euler turbomachine equations.

6.3 Blowing Parameter Selection

The intensity of pre-whirl added through blowing is parameterized with three variables: 1) a polar angle, 2) an azimuthal angle, and 3) volumetric flow rate. See Figure 38. Blowing through the jets is fully defined by these parameters. The polar and azimuthal angles are specified relative to the wall of the draft tube cone. The polar angle is defined as the angle between the jet inlet velocity vector and a plane perpendicular to the axis of rotation. Positive polar angles add axial velocity to the bulk flow in the draft tube cone. The azimuthal angle is defined as the angle between the jet inlet velocity vector and a plane that passes through the axis of rotation. Positive azimuthal angles add pre-whirl to the flow in the direction of impeller rotation. Negative azimuthal angles add pre-whirl in the opposite direction. The flow rates, Q_{jet}, through jets dictate the blowing intensity.

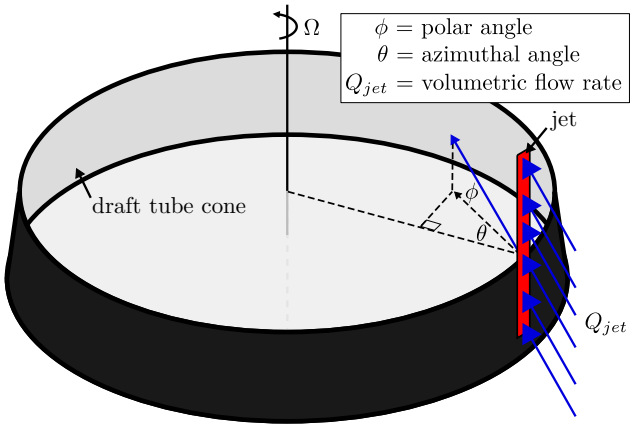

Figure 38. Parameters that control blowing.

Three levels of each control variable are selected for testing. The polar and azimuthal angles are set at 20°, 40° and 60°. Discharge flow rates through the impeller are maintained at a constant level with and without blowing. During blowing, 0.5 %, 1.5 % and 2.5 % of the total flow is redirected through the jets. The performance of each case is measured and compared to base cases without blowing. Jet power is included in the efficiency calculations as a head loss.

6.4 Taguchi Test Matrix

Testing all three levels of peripheral swirl, axial flow, and blowing intensity would show the combination of variables that results in the highest efficiency. However, testing all 27 scenarios is too computationally expensive and not practical. An orthogonal test matrix is used to reduce the number of required simulations from 27 to 9 while still testing all parameters. A summary of the input parameters tested at each flow rate is given in Table 5.

Table 5. Taguchi L4 Orthogonal Test Matrix.

No.	ϕ	θ	$\%Q$
1	20	20	0.5
2	20	40	1.5
3	20	60	2.5
4	40	20	1.5
5	40	40	2.5
6	40	60	0.5
7	60	20	2.5
8	60	40	0.5
9	60	60	1.5

Each scenario in Table 5 is tested at four flow rates: Case01, Case04, Case05, and Case06. The nine jet inlet boundary conditions are tested using frozen rotor simulations. Head rise is measured across the pump impeller at section DD and section AA, and pump efficiencies are calculated according to the definition in Equation 24.

In each case, the average of each level within a parameter is calculated. The average of each level is subtracted from the grand average of all levels of a parameter. The relative difference between level averages and grand averages is shown in Figure 39. For example, in Case05 the effect of flow rate is greater than the global mean at level one, less than the global mean at level two, and almost equal to the global mean at level three. By contrast, the effect of the polar angle is near the global mean at all three levels. The effect of azimuthal angle is also close to the global mean, but decreases from level one to level three.

The analysis of steady state results yields no clear improvement in efficiency. Changes of less than one percent in efficiency are observed when pre-whirl conditions exist. The levels of each parameter are selected to maximize efficiency. Using Case05 as an example again, level one is selected for all parameters because they produce the greatest gain in efficiency compared to the global average. The selected levels for all case are listed in Table 6. These selected levels are used to determine inlet boundary conditions of full-wheel moving mesh simulations.

Taguchi signal-to-noise ratios are calculated to determine the effect each variable has on efficiency. The

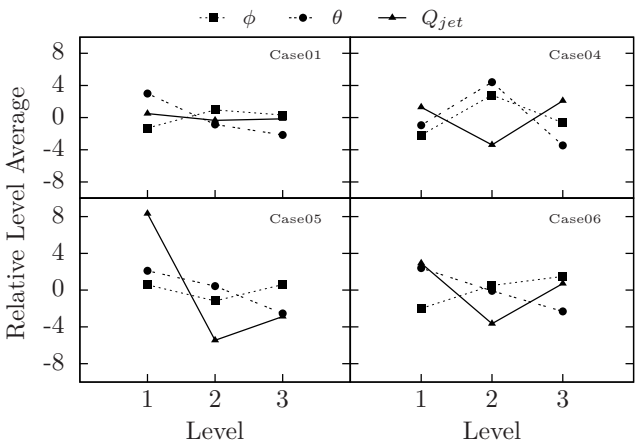

Figure 39. Taguchi level averages for relative efficiency.

Table 6. Selected Parameter Levels.

Case	ϕ	θ	$\%Q_{BEP}$
Case01	40	20	0.5
Case02	60	20	0.5
Case04	40	40	2.5
Case05	40	20	0.5
Case06	60	20	0.5

ranges of signal-to-noise level averages show that of the three parameters tested, the flow rate through the jets has the greatest effect on pump efficiency. This result is expected because hydraulic losses from flow through the jets have a direct impact on pump performance. Azimuthal swirl angle is also a significant indicator of pump efficiency, as expected from the Euler turbomachinery equation. The polar angle, and by extension added axial velocity, has little impact on efficiency.

6.5 Pump Performance

Figure 40 shows normalized head and efficiency from steady state analysis using multiple reference frames, transient full-wheel CFD simulations, and experimental results provided by the manufacturer. As expected, steady state simulations overpredicted losses when modeling the rotor-stator interaction and flow in the spiral case. Transient simulations provid more accurate assessments of pump efficiency. Data points correspond to test cases listed in Table 4.

The solid curves are smoothed test data from model tests of the pump. A scale factor is used to map model performance to prototype performance predicted in the figure. The region of unstable pump operation is apparent as the flat head curve between $\Phi = 0.015$ to $\Phi = 0.05$ in Figure 40. Case01 and Case02 are well outside the normal operating range and in the region of pump instability. Additional losses due to unstable flow in this region cause efficiency to be under predicted for all simulations.

Curves with square symbols are calculated from frozen rotor simulations without any added pre-whirl. Multiple reference frames are used to account for impeller rotation. Head rise through the pump is under predicted. Therefore, efficiency is also lower. Losses arise from poor flow conditions in the spiral case due to the rotor-stator interface.

Curves with circle symbols are calculated from moving mesh simulations with a time step of 0.001 s. The rotor mesh advances 1.2° every time step. Each simulation is run for a minimum of three complete revolutions. Moment and pressure measurements converge within this time. Efficiency agrees with expected results in the normal range of operation. However, the efficiency is underpredicted at small discharge outside the normal operating range, as seen in Case01 and Case02. The difference between the calculated head and actual head is approximately 5 % error and occurs in Case05.

Curves with triangle symbols are calculated with added positive pre-whirl. Head is unchanged near the design flow rate (Case04). However, head drops at discharge higher than the design flow rate and rises at discharges lower than the design point.

Curves with diamond symbols are calculated with reverse pre-whirl. That is, the azimuthal angle at the jet inlet is negative and the pre-whirl is in the opposite sense direction as impeller rotation. Head is unchanged near the design flow rate. Head increases at higher flow rates, and a small improvement in efficiency is observed. Head decreases sightly in Case02, but changes in efficiency are not significant.

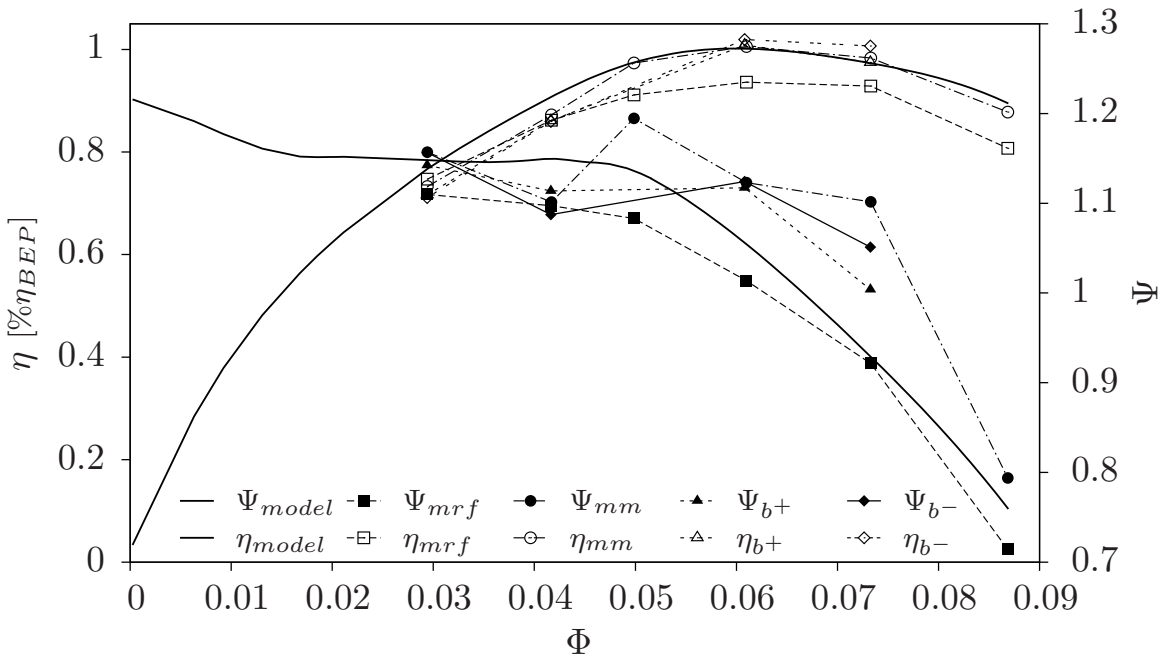

Figure 40. Head and efficiency for all test cases.

6.6 Pressure Pulsations

An FFT analysis of time-dependent pressure levels at monitoring locations in the draft tube and at surfaces of guide vane and spiral case walls reveal the blade passing frequency. The impeller blades and spiral case guide vanes have an integer common factor of three. In this case, subharmonics with respect to the rotor and stator produce larger pressure pulsations at approximately 6 Hz and 10 Hz than the fundamental rotating frequency at 3.3 Hz. The blade passing frequency magnitudes of 30 Hz and the first harmonic of 60 Hz dominate the frequency spectrum. Figure 41 show these frequencies with respect to typical frequency ranges found in hydro turbines.

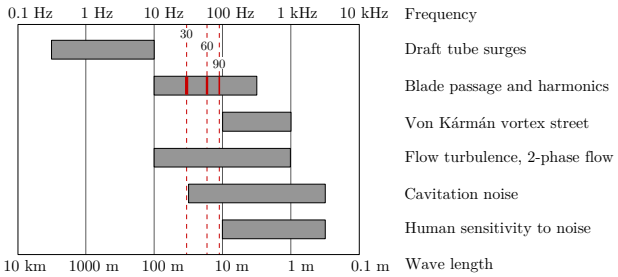

Figure 41. Typical frequency ranges in hydro turbines. The blade passing frequency (30 Hz) and the first and second harmonics are shown in red. Adapted from source: [51].

Figure 42 shows the pulsations in the penstock compared with test data obtained by Frizell [52]. Frizell monitors strain in the penstock by attaching strain gauges at the locations shown in the figure. Measurements are taken for 10.24 min at a sample rate of 1000 Hz.

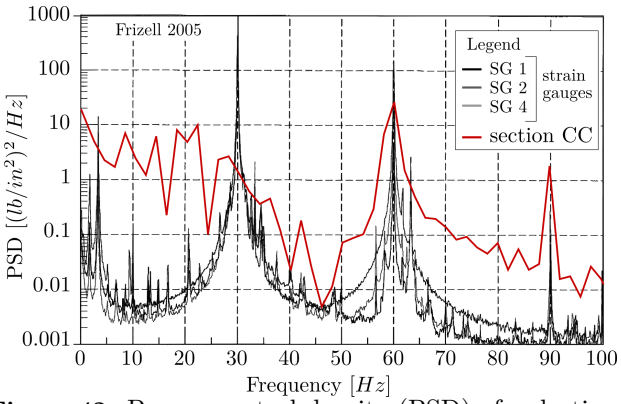

Figure 42. Power spectral density (PSD) of pulsations in the penstock during steady state operation of pump No. 2 at the Grand Coulee pumping station. Adapted from source: [52].

7. Conclusion

The results are inconclusive and no clear improvement in efficiency is detected. This is primarily due to the choice of blowing intensity which is not sufficient to alter the angular momentum of the flow in the draft tube cone. Parasitic losses from the jets at off-design conditions are small and appear to be offset by the added momentum at the inlet of the pump. Transient flow in the impeller passage and spiral case at low discharge are not improved with the levels of added pre-whirl.

Additional simulations with greater blowing intensity

could be run to increase the magnitude of the pre-whirl effect. A larger net effect would aid in the identification of benefits of inlet whirl. Running more simulations near the instable flow conditions would generate a more accurate operating envelope. This type of systematic investigation would need to be carried out on a smaller grid to maintain a reasonable computational expense. A large saving in computational time could be achieved by only modeling a single blade passage and periodic spiral case section. Finally, other turbulence models, such as $k - \epsilon$, could be used to better predict losses in the unstable operating region.

Acknowledgments

This project is supported by The Hydro Research Foundation through a grant from the United States Department of Energy.

References

[1] Vernon M. Murray. Grand Coulee and Bonneville Power in the National War Effort. *The Journal of Land & Public Utility Economics*, 18(2):pp. 134–139, 1942.

[2] USACE. *A History of the US Army Corps of Engineers Hydroelectric Design Center, 1938-2005*. United Sates Army Corps of Engineers, 2005.

[3] EIA. 2011 Form EIA-860 Data - Schedule 3, 'Generator Data' (Operable Units Only). U.S. Energy Information Administration, January 2013. Final 2011 data.

[4] EIA. Net Generation: Conventional Hydroelectric: All Sectors 2012. U.S. Energy Information Administration Electricity Data Browser, 2013.

[5] 2013. Personal communication with representatives from Weir American Hydro.

[6] JL Gordon. Hydraulic turbine efficiency. *Canadian Journal of Civil Engineering*, 28(2):238–253, 2001.

[7] Jessica Manness and Jay Doering. An improved model for predicting the efficiency of hydraulic propeller turbines. *Canadian Journal of Civil Engineering*, 32(5):789–795, 2005.

[8] H. Keck and M. Sick. Thirty years of numerical flow simulation in hydraulic turbomachines. *Acta Mechanica*, 201(1):211–229, 2008.

[9] Boualem Hadjerioua, Yaxing Wei, and Shih-Chieh Kao. An Assessment of Energy Potential at Non-Powered Dams in the United States. Technical Report DE-AC05-00OR22725, Oak Ridge National Laboratory, Oak Ridge, Tennessee 37831, 2012.

[10] Hydropower Analysis Center. Hydropower Resource Assessment at Non-Powered USACE Sites. Technical report, Hydropower Analysis Center, United States Army Corps of Engineers, July 2013.

[11] Power Resources Office, United States Bureau of Reclamation. Reclamation Managing Water in the West: Hydropower Resource Assessment at Existing Reclamation Facilities. Technical report, United States Bureau of Reclamation, March 2011.

[12] Hall G. Douglas and Kelly S. Reeves. A Study of United States Hydroelectric Plant Ownership. Technical Report INL/EXT-06-11519, Idaho National Laboratory, June 2006.

[13] EIA. Electric Power Annual 2011. Technical report, United States Energy Information Administration United States Department of Energy, January 2013. Table 4.3. EIA-860 Annual Electric Generator Report.

[14] DOE. 2012 Wind Technologies Market Report. Technical report, United States Department of Energy, August 2013.

[15] EIA. Annual Energy Outlook 2013 with Projections to 2040. U.S. Energy Information Administration, 2013.

[16] Abbas A. Akhil, Georgianne Huff, Aileen B. Currier, Benjamin C. Kaun, Dan M. Rastler, Stella Bingqing Chen, Andrew L. Cotter, Dale T. Bradshaw, and William D. Gauntlett. DOE/EPRI 2013 Electricity Storage Handbook in Collaboration with NRECA. Technical Report SAND2013-5131, Sandia National Laboratories, July 2013.

[17] PJM. Hourly Load Data, August 2013.

[18] Brad Roberts and Jessica Harrison. Energy Storage Activities in the United States Electricity Grid. Technical report, Electricity Advisory Committee and U.S. Department of Energy, May 2011.

[19] EIA. 2012 Form EIA-860 Data - Schedule 3, 'Generator Data' (Operable Units Only). U.S. Energy Information Administration, October 2013. Final 2012 data.

[20] E.ON. Graphic presentation of the power plant assemblies at the Waldeck site. E.ON SE, 2013. Pumped storage power station layout.

[21] Olivier Teller. Flexible large-scale pumped hydroelectric energy storage. In *Session 1: "Electric energy storage options for variable renewable energy sources - Today's situation"*, Seville, Spain, November 2012. Alstom, International Partnership for Hydrogen and Fuel Cells in the Economy Workshop.

[22] Sundar Venkataraman, Gary Jordan, Richard Piwko, Lavelle Freeman, Udi Helman, Clyde Loutan, Grant Rosenblum, Mark Rothleder, June Xie, Hong Zhou, Michael Kuo, Jian Ma, Yuri Makarov, Tao Guo, Wenxiong Huang, Eric Toolson, Anupama Pandey,

Barney Speckman, and Paul Worhach. Integration of Renewable Resources Operational Requirements and Generation Fleet Capability at 20% RPS. California Independent System Operator Corporation, August 2011.

[23] USACE. Hourly Project Data. U.S. Army Corps of Engineers, 2013. Grand Coulee generating and pumping data.

[24] USACE. Columbia Basin Data Archives. U.S. Army Corps of Engineers, 2013. Historic Grand Coulee generating data.

[25] Michael CW Kintner Meyer, Patrick J Balducci, Chunlian Jin, Tony B Nguyen, Marcelo A Elizondo, V Viswanathan, Xinxin Guo, and F Tuffner. Energy Storage for Power Systems Applications: A Regional Assessment for the Northwest Power Pool (NWPP). Technical Report PNNL-19300, Pacific Northwest National Laboratory, 2010.

[26] David Connolly, Henrik Lund, P Finn, Brian Vad Mathiesen, and M Leahy. Practical operation strategies for pumped hydroelectric energy storage (PHES) utilising electricity price arbitrage. *Energy Policy*, 39(7):4189–4196, 2011.

[27] M Kintner Meyer, P Balducci, W Colella, M Elizondo, C Jin, T Nguyen, V Viswanathan, and Y Zhang. National Assessment of Energy Storage for Grid Balancing and Arbitrage: Phase 1, WECC. Technical Report PNNL-21388, Pacific Northwest National Laboratory, June 2012.

[28] J Heeter, G Barbose, L Bird, S Weaver, F Flores-Espino, K Kuskova-Burns, and R Wiser. A survey of state-level cost and benefit estimates of renewable portfolio standards. Technical Report NREL/TP-6A20-61042, National Renewable Energy Laboratory (NREL), May 2014.

[29] John S Anagnostopoulos and Dimitris E Papantonis. Pumping station design for a pumped-storage wind-hydro power plant. *Energy Conversion and Management*, 48(11):3009–3017, 2007.

[30] Lei Tan, ShuLiang Cao, and ShaoBo Gui. Hydraulic design and pre-whirl regulation law of inlet guide vane for centrifugal pump. *Science China Technological Sciences*, 53(8):2142–2151, August 2010.

[31] Lei Tan, ShuLiang Cao, YuMing Wang, and BaoShan Zhu. Influence of axial distance on prewhirl regulation by the inlet guide vanes for a centrifugal pump. *Science China Technological Sciences*, 55(4):1037–1043, 2012.

[32] CM Zhou, HM Wang, X Huang, and H Lin. Influence of the positive prewhirl on the performance of centrifugal pumps with different airfoils. In *IOP Conference Series: Earth and Environmental Science*, volume 15, page 032020. IOP Publishing, 2012.

[33] Jun Xiao, Chuangang Gu, Xinwei Shu, and Chuang Gao. Performance analysis of a centrifugal compressor with variable inlet guide vanes. *Frontiers of Energy and Power Engineering in China*, 1(4):473–476, 2007.

[34] USBR. Grand Coulee Dam Statistics and Facts. U.S. Department of the Interior Bureau of Reclamation, March 2012.

[35] S. L. Dixon and C. A. Hall. *Fluid Mechanics and Thermodynamics of Turbomachinery*. Butterworth-Heinemann, Elsevier Inc., sixth edition, 2010.

[36] Andritz. Vertical volute pumps, 2010.

[37] Johann Friedrick Gulich. *Centrifugal Pumps*. Springer, 2007. ISBN 978-3-540-73694-3.

[38] USBR. John W. Keys III Pump-Generating Plant. U.S. Department of the Interior Bureau of Reclamation, March 2011.

[39] S. M. Denton. Irrigation Pumping with Grand Coulee Power. *AIEE Transactions*, 67:1362–1368, 1948.

[40] Jens M Österlund. *Experimental studies of zero pressure-gradient turbulent boundary layer flow*. PhD thesis, Royal Institute of Technology, 1999.

[41] HDR. Grand Coulee / John Keys Pumping Plant Summary Assessment and Upgrade Review. Technical report, Bonneville Power Administration, June 2010.

[42] ANSYS. *ANSYS FLUENT Theory Guide*. ANSYS, Inc., release 14.0 edition, November 2011.

[43] Lewis Fry Richardson. The approximate arithmetical solution by finite differences of physical problems involving differential equations, with an application to the stresses in a masonry dam. *Royal Society of London Philosophical Transactions Series A*, 210:307–357, 1911.

[44] Lewis F Richardson. The deferred approach to the limit. Part I. Single lattice. *Philosophical Transactions of the Royal Society of London. Series A, containing papers of a mathematical or physical character*, pages 299–361, 1927.

[45] W. L. Oberkampf and C. J. Roy. *Verification and Validation in Scientific Computing*. Cambridge University Press, New York, 2010.

[46] Ishmail B Celik, Urmila Ghia, Patrick J Roache, et al. Procedure for estimation and reporting of uncertainty due to discretization in cfd applications. *Journal of Fluids Engineering of the ASME*, 130(7), July 2008.

[47] CJ Freitas, Urmila Ghia, I Celik, P Roache, and P Raad. ASME's quest to quantify numerical uncertainty. *AIAA Paper*, 627:2003, 2003.

[48] Patrick J Roache. Perspective: a method for uniform reporting of grid refinement studies. *Journal of Fluids Engineering*, 116(3):405–413, 1994.

[49] Patrick J Roache. Verification of codes and calculations. *AIAA journal*, 36(5):696–702, May 1998.

[50] Patrick J Roache. Error bars for CFD. *AIAA paper*, 408:2003, 2003.

[51] Peter Dörfler, Mirjam Sick, and André Coutu. *Flow-Induced Pulsation and Vibration in Hydroelectric Machinery*. Springer, 2013.

[52] Warren K. Frizell. Dynamic Study of the P2 Discharge Line at Grand Coulee Pumping Plant. Data transmittal report, U.S. Bureau of Reclamation, Denver, Colorado, December 2005. Water Resources Research Laboratory.